HHS Public Access

Author manuscript

Cell Stem Cell. Author manuscript; available in PMC 2019 January 24.

Published in final edited form as:

Cell Stem Cell. 2018 May 03; 22(5): 684–697.e9. doi:10.1016/j.stem.2018.04.009.

Efficient Generation of CA3 Neurons from Human Pluripotent Stem Cells Enables Modeling of Hippocampal Connectivity *In Vitro*

Anindita Sarkar[1,*], **Arianna Mei**[1], **Apua C.M. Paquola**[1,2], **Shani Stern**[1], **Cedric Bardy**[1,3], **Jason R. Klug**[4], **Stacy Kim**[1], **Neda Neshat**[1], **Hyung Joon Kim**[1,5], **Manching Ku**[6,10], **Maxim N. Shokhirev**[7], **David H. Adamowicz**[1,8], **Maria C. Marchetto**[1], **Roberto Jappelli**[1], **Jennifer A. Erwin**[1,2], **Krishnan Padmanabhan**[1,9], **Matthew Shtrahman**[1,8], **Xin Jin**[4], and **Fred H. Gage**[1,11,*]

[1]Laboratory of Genetics, Salk Institute for Biological Studies, 10010 North Torrey Pines Road, La Jolla, CA 92037, USA

[2]The Lieber Institute for Brain Development, Johns Hopkins School of Medicine, 855 N Wolfe Street, Baltimore, MD 21205, USA

[3]Laboratory for Human Neurophysiology and Genetics, SAHMRI and College of Medicine and Public Health, Flinders University, Adelaide SA 5000, Australia

[4]Molecular Neurobiology Laboratory, Salk Institute for Biological Studies, 10010 North Torrey Pines Road, La Jolla, CA 92037, USA

[5]Department of Psychiatry, Mary and Dick Holland Regenerative Medicine Program, University of Nebraska Medical Center, Omaha, NE 68198-5965, USA

[6]Next Generation Sequencing Core, Salk Institute for Biological Studies, 10010 North Torrey Pines Road, La Jolla, CA 92037, USA

[7]Razavi Newman Integrative Genomics and Bioinformatics Core Facility, Salk Institute for Biological Studies, 10010 North Torrey Pines Road, La Jolla, CA 92037, USA

[8]Department of Neurosciences, UCSD School of Medicine, 9500 Gilman Drive, La Jolla, CA 92093, USA

[9]The Ernest J. Del Monte Institute for Neuroscience, University of Rochester School of Medicine and Dentistry, 601 Elmwood Avenue, Box 603, Rochester, NY 14642, USA

[*]Correspondence: anindsarkar@gmail.com (A.S.), gage@salk.edu (F.H.G.).

AUTHOR CONTRIBUTIONS

Conception, design, and writing of the manuscript, A.S. and F.H.G.; neuronal differentiation and other cellular and molecular assays, A.S.; bioinformatics analysis, M.N.S and A.C.M.P.; library preparation and sequencing of singlecell RNA, A.S. and M.K.; cell transplantation, A.S., K.P., S.K., and M.S.; whole-cell patch-clamp, C.B., S.S., J.R.K., and X.J.; reagent contribution, H.J.K., D.H.A., R.J., M.C.M., and J.A.E.; data analysis and interpretation, contribution to experimental design, and editing of the manuscript, A.S., A.M., N.N., M.N.S., A.C.M.P., H.J.K., C.B., S.S., J.R.K., X.J., and F.H.G.

DECLARATION OF INTERESTS

The authors declare no competing interests.

SUPPLEMENTAL INFORMATION

Supplemental Information includes seven figures and three tables and can be found with this article online at https://doi.Org/10.1016/j.stem.2018.04.009.

A video abstract is available at https://doi.org/10.1016/j.stem.2018.04.009#mmc5.

[10]Present address: Department of Hematology-Oncology, University of Freiburg, 79106 Freiburg, Germany

[11]Lead Contact

SUMMARY

Despite widespread interest in using human induced pluripotent stem cells (hiPSCs) in neurological disease modeling, a suitable model system to study human neuronal connectivity is lacking. Here, we report a comprehensive and efficient differentiation paradigm for hiPSCs that generate multiple CA3 pyramidal neuron subtypes as detected by singlecell RNA sequencing (RNA-seq). This differentiation paradigm exhibits characteristics of neuronal network maturation, and rabies virus tracing revealed synaptic connections between stem cell-derived dentate gyrus (DG) and CA3 neurons *in vitro* recapitulating the neuronal connectivity within the hippocampus. Because hippocampal dysfunction has been implicated in schizophrenia, we applied DG and CA3 differentiation paradigms to schizophrenia-patient-derived hiPSCs. We detected reduced activity in DG-CA3 co-culture and deficits in spontaneous and evoked activity in CA3 neurons from schizophrenia-patient-derived hiPSCs. Our approach offers critical insights into the network activity aspects of schizophrenia and may serve as a promising tool for modeling diseases with hippocampal vulnerability.

Graphical Abstract

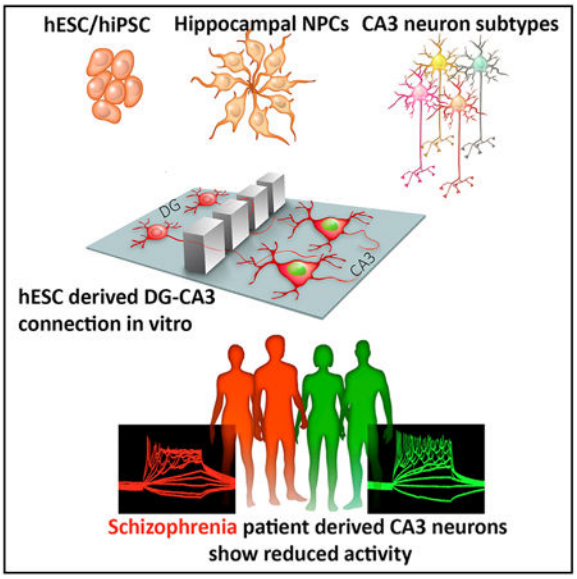

In Brief

Sarkar et al. established a differentiation paradigm that generates human CA3 pyramidal neurons from ESCs and iPSCs and recapitulates hippocampal connectivity *in vitro*. This work reveals reduced levels of activity of schizophrenia-patient-derived neurons, offering opportunities for modeling diseases with hippocampal vulnerability.

INTRODUCTION

Neural connections underlie human brain function. Dysfunction of neural connections weakens the efficiency of information transfer and correlates with the progression of neurological disorders. While in the past, our understanding of neuronal communication has come mainly from animal models, the development of pluripotent stem cell technologies has enabled us to generate lineage-specific human neurons *in vitro*. Tremendous progress has been made using these neurons to understand disease etiologies. However, a majority of the current diseasemodeling studies focuses on individual cell types rather than the network they are embedded in, as robust *in vitro* assay to study lineage-specific human neuronal connection remains an experimental challenge.

The hippocampus is an ideal structure for modeling the development and functioning of the neuronal network. Hippocampal cell types, molecular boundaries, and circuit organization have been particularly well studied. Furthermore, the hippocampus is a highly plastic region sensitive to environmental stimuli and shows vulnerability to a growing list of neurological disorders (Small et al., 2011). The mossy fiber (MF) pathway, through which presynaptic dentate gyrus (DG) axons connect to postsynaptic CA3 neurons, is subjected to constant modifications during development and throughout life, making it an attractive candidate to model neurodevelopmental disorders such as schizophrenia (SZ). SZ is a heterogeneous disorder that involves alterations in neuronal connectivity in the prefrontal cortex and other cortical brain regions (Akbarian et al., 1995; Hashimoto et al., 2003). Diminished encoding of verbal declarative memory, a hippocampus-dependent function, is consistently reported in SZ patients, unaffected relatives, and at-risk individuals (Cirillo and Seidman, 2003; Rasetti et al., 2014). Postmortem studies have revealed reductions in synapse density in CA3 (Kolomeets, 2007; Kolomeets et al., 2007) and decreased glutamate transmission in DG (Li et al., 2015; Tamminga et al., 2010; Tamminga and Zukin, 2015). Together, these observations suggest a plausible role of structural and functional alterations of the MF circuit in the pathogenesis of SZ. On the other hand, studies using differentiated neurons from SZ and healthy induced pluripotent stem cell (iPSC) lines revealed deficit in migration, polarity, synaptic maturation, and activity of SZ neurons (Brennand et al., 2011, 2015; Robicsek et al., 2013; Wen et al., 2014; Yu et al., 2014). Despite these findings, an *in vitro* model that facilitates the study of human neuronal network properties in the modeling of SZ and other neurodevelopmental disorders is lacking, and assays that can be used to quantitatively measure development and functions of the neuronal connection between synaptic pairs remain inadequately developed. In the present study, we established a protocol to differentiate hippocampal CA3 pyramidal neurons and developed an *in vitro* model to assay the iPSC-derived hippocampal DG-CA3 circuit.

During development, Wnt signaling regulates cell proliferation and fate specification of DG and cornu ammonis (CA) fields of the hippocampus (Galceran et al., 2000; Lee et al., 2000). For instance, in mutants for Wnt3a or downstream effector Lef1, both DG- and CA field-specific markers are mostly absent. Wnt3a has been previously utilized in specifying human (h) DG cells from hESC/iPSC-derived neuronal progenitors (Sakaguchi et al., 2015; Yu et al., 2014). Similarly, Ka1 (Grik4), a gene enriched in CA3, was found to be expressed in neurons derived from Wnt3a-treated 3D organoids (Sakaguchi et al., 2015).

Herein, we report a comprehensive CA3 patterning from embryonic stem cells (ESCs) and iPSCs that results in functionally mature CA3 neurons, including a subtype present in human, but not in mouse: secretagogin (SCGN)-expressing CA3 neurons. ESC/iPSC-derived DG neurons connect with these CA3 neurons, recapitulating a human hippocampal MF connection *in vitro*. Importantly, the CA3 and DG-CA3 populations reveal spontaneous and evoked activity deficits in SZ, suggesting that a reduction in activity in the MF circuit may be involved in SZ pathology.

RESULTS

An *In Vitro* Differentiation Protocol for Generating Hippocampal CA3 Neurons

To identify the suitable neuronal progenitor cells (NPCs) for CA3 differentiation, we used previously published protocols to differentiate hESCs (huES6) to derive both the pan-NPC and hippocampus-patterned NPCs (hpNPCs) (Marchetto et al., 2016; Yu et al., 2014). Combined inhibition of the wnt, tgfß, shh, and bmp pathways induced the generation of hpNPCs. We compared the transcriptome of these pan and hpNPC populations by next-generation RNA sequencing (RNA-seq). A large number of genes were differentially regulated in these two populations (Figure 1A; Table S1). Orthodenticle homeobox 2 (*Otx2*), a marker of the cortical hem (Kimura et al., 2005), was the top upregulated gene in the hpNPC population (Table S1). An antibody against OTX2 and OTX1 validated the upregulation of OTX in hpNPCs (Figures 1B and 1C). In addition to OTX2, hpNPCs showed enrichment of several cortical hem markers such as *Zic2, Emx2, Wnt2b*, and *Wnt3a* (Figure S1A) and a number of Wnt signaling molecules (Figure 1E), recapitulating the Wnt-rich medial pallium that gives rise to the hippocampus.

We further treated the hpNPCs with recombinant WNT3A to induce CA3 differentiation. DG primordia lie next to the cortical hem and presumably are exposed to high levels of Wnt3a, whereas, further dorsally, CA3 primordia is exposed to a correspondingly lower end of the Wnt3a gradient (Figure 1D). NPCs were treated with differentiation media containing 5 ng WNT3A (instead of the 20 ng used in the $PROX1^+$ hDG protocol), in addition to BDNF, ascorbic acid and cyclic AMP (cAMP) for the first 3 weeks. This treatment was followed by 1–6 weeks of differentiation without WNT3A (Figure 1F). At 6 weeks *in vitro* (WIV), the majority of the differentiated neurons in the low WNT3A-treated culture were $VGLUT1^+$ $NeuN^+$ glutamatergic neurons (>90%) (Figure 1G), and ~75% of the $MAP2^+$ neurons expressed GRIK4, a well-known CA3-specific gene (Figure 1H).

To characterize the differentiated neurons, we performed RNA-seq analysis on the transcriptome of 6-week-old hCA3s and hpNPCs (Table S2). Our analysis revealed upregulation of >20 genes in hCA3s, with known enriched expression in human and rodent CA3 and CA2 (Thompson et al., 2008; Zhao et al., 2001) (Figure 2A). qRT-PCR validated upregulation of expressions of *Pvrl3, Dkk3, TGFβ2*, and *Grik4* (Figures S2B and S2C). The upregulated genes include markers that were known to express in the broad CA3 field (or both CA3 and CA2 fields) (*Elavl2* and *Grik4*) as well as by subsets of CA3 neurons (*Prkcd*) (Iwano et al., 2012; Thompson et al., 2008). While the mechanism leading to subtype specification is presently unclear, recent findings have started to reveal that the CA field within the hippocampus shows a high degree of heterogeneity. Several genes have been

reported to have region-restricted expression patterns that might underlie different afferent and efferent connectivity (Thompson et al., 2008; Zhao et al., 2001). Importantly, when compared to a pan-neuronal transcriptome at an equivalent stage of differentiation (Marchetto et al., 2016), the enrichment of CA3 genes was found to be specific in the hCA3 transcriptome (Figure 2C). In contrast to the enrichment of these genes expressing in CA3 (and CA2), markers for other hippocampal neuronal classes such as DG (*Calb1, Prox1, C1ql2*, and *Dock10*) or CA1 (*Pou3f1*) were not consistently enriched in 6-week-old hCA3s (Figure 2B). Furthermore, immunostaining of ELAVL2, SCGN, and PRKCD confirmed the presence of significantly higher numbers of CA3 neurons in hCA3 compared to hDG (Figures 2C and 2D). On the other hand, only a small fraction of neurons in hCA3 expressed CALB1 (~10%), a marker for DG neurons (>75%) Figures 2C, 2D, and S1E. Similarly, CTIP2, a marker for DG, CA1, and cortical neurons (Williams et al., 2011), was not expressed in a majority of CA3 neurons (~90%) (Figure S1D). GABA, an inhibitory interneuron marker, was present equally (<12%) in both hCA3 and hDG populations (Figure 2C). Together, these results indicated that low Wnt-dependent differentiation of hpNPCs resulted in a heterogeneous CA3 neuron population.

Molecular Census of the hCA3 Population

We used single-cell transcriptome analysis to perform a molecular census on a 2-week-old differentiating hCA3 population derived from huES6 hpNPCs. A population containing more than 85% viable cells was subjected to cell lysis and encapsulations and prepared for single-cell RNA-seq using SureCell WTA 3′ Library Prep Kit for the ddSEQ System (Illumina and Bio-Rad). Cells with normalized read counts in the lower quartile were filtered (optimized based on the distribution of cell counts) resulting in 380 high-quality cells (Figures S2A and 2B). Next, a CPM normalization was applied, and genes with zero reads were removed, resulting in 17,388 expressed genes. A t-distributed stochastic neighbor embedding (tSNE) plot was constructed to visualize the cells in a reduced-dimensionality space, and silhouette analysis was used to find the 3 optimal k-means clusters for the cells in 2D tSNE space (green, blue, and red) (Figures 3A and S2C). The green cluster was a relatively smaller cluster and was separated from the rest along the tSNE1 axis. All the clusters consisted of neurons (average expression of both mature and immature markers: *Map2, Nefl, Tuj1, Rbfox3*, and *Dcx*) (Figures 3B and S2F), whereas neural progenitors such as *Sox2* (Figure 3B), *Nes*, and *S100b* (Figures S2D and S2E) were enriched in the red and blue clusters.

CA3 neurons (as defined by the average expression of 23 CA3 genes) were highly enriched in the green cluster (Figure 3C). To identify differentially expressed genes between the green cluster and others, we used the edgeR differential expression pipeline, treating all cells within the cluster as replicates and comparing to all other cells. We found 1,628 differentially expressed genes in the green cluster, including 326 genes upregulated, and 1,302 genes downregulated (false discovery rate [FDR] < 0.05 and log2fold > 1) compared to all other cells (Table S3). Markers with known hippocampal expression such as *Lhx9, Lhx2, Elavl2*, and *Tspan7* were upregulated in the green cluster (Figure 3D) (Abellán et al., 2014; Arnold and Trojanowski, 1996; Bertuzzi et al., 1999; He et al., 2012; Miller et al., 1993; Stranahan et al., 2010). In contrast, many downregulated genes (e.g., *Apoe*) have been

shown to be absent in mouse CA3 (Xu et al., 2006). Additionally, genes encoding ion channels, transporters such as *Scn2a, Scn3b, Cacna1b*, and *Vglut2*, were upregulated (Figure 3D). To further understand the biological functions of the differentially expressed genes (DEGs), enrichment analyses based on Gene Ontology (GO) and Kyoto Encyclopedia of Genes and Genomes (KEGG) pathways were performed using metascape (http://metascape.org) (Tripathi et al., 2015). When the DEGs between all the clusters (1,628 DEGs) were checked against the GO database, ~1,900 GO terms were significantly enriched. The GO term assigned the largest number of upregulated genes (29) was ‘‘cell projection morphogenesis’’ (GO: 0048858), followed by ‘‘chemical synaptic transmission’’ (GO: 0007268), and ‘‘neuron migration’’ (GO: 0001764) (Figure 3E). The GO terms assigned to the downregulated genes were regulation of Wnt signaling pathway and embryonic morphogenesis among others. There were no upregulated genes in the red cluster, and the blue cluster had only 2 downregulated genes (Table S3). Wnt signaling induces both proliferation and fate specification of hippocampal neurons *in vitro*, and the 2-week-old hCA3 population includes both proliferating NPCs and terminally differentiated neurons. The green cluster within the hCA3 population might represent a developmental stage where the pathways for neuronal projection and synapse formation are enriched, and CA3 neuronal genes are already expressed. A comparison with the bulk hCA3 transcriptome (hpNPCs and hCA 3–6 WIV; Table S2) showed an overwhelming majority of ‘‘up’’ genes, but not ‘‘down’’ genes, were upregulated during early hpNPC-hCA3 differentiation (Figures S2G). For instance, immunostaining of LHX9 confirmed a higher expression in hCA3s (4 WIV) compared to proliferating hpNPCs (Figure 3F).

hCA3 Constitutes a Heterogeneous Population

While CA1 (as defined by *Wfs1* and *Pou3f1* expression) and CA2 (as defined by *Pcp4* and *Rgs14* expression) neurons did not cluster together (Figure 4A), CA3 neurons were enriched in the green cluster (Figure 3C). However, individual CA3 genes showed heterogeneous expression patterns (Figure 4C). For example, a substantial fraction of cells expressed *Elavl2* and *Snca*, but the majority of the cells did not co-express those genes (Figure 4C). On the other hand, neuronal genes (*Map2* and *Dcx*) and housekeeping genes (*Actb* and *Tub1a1*) were expressed more broadly and in an overlapping population (Figure 4B).

We also observed sparse expression of a few CA3 genes (e.g., *Tgfb2* and *Scgn*) (Figure 4D). Scgn is a member of Ca^{2+}-binding protein (CaBP) family, containing the characteristic 6 helix-loophelix motifs called EF-hand motifs. Because Scgn was found to be the top upregulated gene in hCA3s (2–6 weeks) (Table S2), we explored *Scgn* expression in CA3. The sparse expression pattern of *Scgn*, as seen in single-cell RNA-seq data, was also observed by immunohistochemistry, as SCGN protein is detected in a small population of hCA3s (~7%–12% of $MAP2^{+}$ neurons in hCA3) (Figure 4E). Intrigued by this sparse expression of both RNA and protein, we performed immunohistochemistry on postmortem human and mouse hippocampal tissue using an antibody that recognized both the human and the mouse protein. This antibody revealed high cell body expression in the human CA3 and CA2 pyramidal layer (Figures 4F and S2H), where DG axons innervated (Kohara et al., 2014), but a low or unidentifiable protein expression in mouse CA3 and CA2 (Figure 4F). Other mouse brain areas such as the amygdala, hypothalamus, and nucleus accumbens

(Figures S2I and S2J) expressed high levels of SCGN. We calculated the ratio of ELAVL2/SCGN neurons in human brain and hCA3, integrating both the highly abundant and the sparse subtypes in the population. This calculation revealed a surprisingly similar ELAVL2:SCGN ratio (Figure 4G) for the hCA3 and the human CA3 neurons, suggesting that the hCA3 population emulates the distribution of these two cell types ($ELAVL2^+$ and $SCGN^+$) in the adult human hippocampus. $SCGN^+$ neurons in mouse nucleus accumbens possessed small soma (Shi et al., 2012). We also observed a smaller soma for $SCGN^+$ neurons (when compared to $ELAVL2^+$) in hCA3 and in the human hippocampus (Figures S2K and S2L). In the single-cell transcriptome dataset, a small fraction of the Elavl2-expressing neurons (~10%) were also found to express Scgn (~50% of $Scgn^+$ population). We could not examine the co-expression of ELAVL2 and SCGN, as the compatible antibodies were not available. Taken together, we provide evidence that hCA3 differentiation results in comprehensive and heterogeneous CA3 patterning, even includes neuronal subtypes with sparse expression, thus making the hCA3s potentially suitable for studying human hippocampal neurotransmission *in vitro*.

Derived hCA3s Mature *In Vitro* and Form a Characteristic Neuronal Network

Differential gene expression analysis of undifferentiated hpNPCs and 2 and 4 WIV hCA3s revealed a robust upregulation of synaptic genes typically found in mature excitatory glutamatergic neurons (Figures S3A and S3B). These include genes encoding AMPA, NMDA, kainate receptors, and voltage-gated potassium and calcium channels (Table S2; Figures S3A and S3B). GO analysis showed an enrichment of GO terms indicative of functional maturation such as positive upregulation of synaptic signaling (GO: 0099536), synaptic transmission (GO: 0007270), and memory (GO: 0007613) (Figure S3C and S3D). GO terms associated with cAMP signaling, memory, and synaptic transmission were consistently upregulated at both 2 and 4 WIV hCA3s.

To examine the electrophysiological properties hCA3s *in vitro*, we performed whole-cell patch-clamp recordings on hCA3 at 6 WIV. We used lentiviral Grik4-EGFP and Elavl2-EGFP reporters to label hCA3 neurons (Figures S4A and S4B) selectively. A total of 10 neurons were analyzed. These neurons demonstrated robust Na^+ and K^+ currents induced by voltage step depolarization (Figure 5A, d). They also showed spontaneous and evoked action potentials (AP) following somatic current injections (Figures 5A, c and e, and Figures S4E–S4T). Furthermore, these neurons showed spontaneous excitatory postsynaptic currents (sEPSCs) in voltage clamp (Figures 5A, f, and Figure S4D), indicating the presence of functional network *in vitro*.

Next, we tested the ability of hCA3s to survive, differentiate, and mature *in vivo* by transplanting hCA3s into the mouse hippocampus. 2-week-old differentiating and immature hCA3 cells were labeled with the lentiviral reporter (Grik4-EGFP and Elavl2-EGFP) and injected into the hippocampus of immunodeficient mice and analyzed at least 3 months post-transplantation (MPT). EGFP-positive cells were detected in the hippocampal CA3 pyramidal layer and adjacent areas (Figures 5B, d, and S4U). We detected $EGFP^+$ cells in mouse hippocampal tissue even after 5.5 MPT, demonstrating the long-term survival of hCA3s (Figures S4U–S4X). At 5.5 MPT, a majority of these grafted cells (>80%) expressed

ELAVL2 and did not express CALB1 and CTIP2 (Figure S4V). Furthermore, consistent with the observation *in vitro*, a small subset of Grik4-eGFP$^+$ hCA3s expressed SCGN (Figures S4W–S4X) in the mouse hippocampus (Figure 3H), where SCGN$^+$ CA3 differentiation is suppressed. Those transplanted hCA3 cells exhibited dense dendritic spines at 5.5 months (Figure S7X).

We assessed the functional properties of hCA3s *in vivo* in comparison to mouse CA3 neurons using whole-cell recordings in acute *ex vivo* hippocampal slices (Figure 5B) using voltage and current clamp at 3–3.5 MPT. A total of 11 cells were targeted for recordings, including 7 non-EGFP mouse CA3s (mCA3) and 4 EGFP$^+$ hCA3s positioned on the pyramidal layer. Both mCA3 and hCA3s exhibited similar resting membrane potential and membrane properties (Figure 5B, m-o). When we compared neuronal excitability, we found that all mCA3s and 50% of hCA3s were able to fire AP trains during somatic current injection and exhibited sodium spikes at depolarized potentials (Figure 5B, g-j). Rheobase current, AP threshold, latency to first AP, and AP amplitude and half-width were not significantly different between mCA3 and hCA3 (Figure 5B, s-w). Additionally, the corresponding current-voltage relationship in current and voltage clamp was not significantly different between hCA3s and mCA3s (Figure 5B, r and x). Overall, these data suggest that hCA3s exhibit similar membrane properties and excitability compared to neighboring mouse neurons.

We next asked whether transplanted cells were able to incorporate into local hippocampal circuits and receive functional excitatory inputs by examining sEPSCs. sEPSCs were readily detected in all cells with no significant difference in the sEPSC frequency or amplitude between transplanted and mouse CA3 neurons (Figure 5B, p and q). These data suggest that hCA3s and mCA3s receive similar numbers of functional excitatory synapses and/or probability of release as well as a similar functional postsynaptic response, respectively. Moreover, these data provide evidence that transplanted neurons can integrate into functional hippocampal circuits *in vivo* receiving functional excitatory inputs.

To develop an *in vitro* model to assay the development and connectivity of the human neuronal network, we next performed repeated multi-electrode array (MEA) recordings on hCA3s. MEA recordings on differentiating hpNPCsto mature neurons (9 WIV) allowed us to collect longitudinal activity at different stages of differentiation and maturation. Compared to the first 3 weeks, there was a significant increase in spontaneous spikes (Figure 5C, a) and increases in the number of active electrodes. Average numbers of bursts (multiple spikes at a single MEA electrode) was also significantly higher in in 4–8 WIV hCA3s than in 0–3 WIV (Figure 5C, b and c). Furthermore, network properties such as numbers of network burst (simultaneous bursts at multiple MEA electrodes) and synchrony index (a measure of synchronous spikes at multiple MEA electrodes) were increased significantly indicating a functionally active hCA3 network at 4–8 WIV (Figure 5C, d and e).

Our results stemmed from *in vitro* disease modeling observations of alterations in synaptic activity in SZ and other disorders (Brennand et al., 2011; Sarkar et al., 2017; Yu et al., 2014). To utilize the mature hCA3s to model the DG-CA3 circuit *in vitro*, we next determined to what extent activity patterns seen *in vitro* were representative of the activity

pattern occurring *in vivo*. We used hDG as a cell type for comparison with hCA3. DG neurons *in vivo* show a low level of intrinsic activity (Gothard et al., 2001; Jung and McNaughton, 1993) with little inter-region connectivity (Amaral et al., 1990). We recorded spontaneous activity in DG and CA3 neurons for 8 weeks using MEA (Figure S4Y). Principal-component analysis on the pooled spontaneous activity data from all the time points successfully separated 2 distinct networks based solely on their spontaneous electrophysiological properties (principal component 1: 98%) (Figure S4Z). Also, the hCA3 spike rate was significantly higher than the DG spike rate (Figure 5D).

To further understand whether this difference in spontaneous activity resulted from a difference in connectivity, we quantified connectivity by using a monosynaptic rabies virus. CA3 pyramidal neurons in mice connect and synapse onto other CA3 neurons via a recurrent excitatory pathway, whereas DG neurons show sparse connectivity among them. Monosynaptic rabies tracing was performed in two steps following the previously published protocol (Brennand et al., 2011). In the first step, infection with a lentiviral reporter with a neuron-specific synapsin promoter expressing rabies G protein and GFP (LV-SYN-G-GFP) required for rabies infection was induced in a small fraction of hCA3s (<15%). In the second step, the culture was infected with G-deficient rabies virus (ΔG-RV). 10 days after rabies infection, we observed GFP^+RFP^+ (postsynaptic), GFP^-RFP^+ (presynaptic), and GFP^+RFP^- (rabies uninfected) neurons in the culture. We compared the connectivity in hCA3 and hDG neuronal cultures by measuring the presynaptic GFP^-RFP^+: postsynaptic GFP^+RFP^+ ratio by fluorescence-activated cell sorter (FACS) analysis. This revealed a significantly higher number of presynaptically connected neurons in the hCA3 population than in the hDG population, indicating a difference in synaptic inputs on hCA3 and hDG neurons (Figure 5E). hCA3s did not show any nonspecific transsynaptic tracing when co-cultured with irradiated mouse fibroblasts (Figure 5E). Our findings showed that hCA3 and hDG activity mimicked gradual neural development and that the hCA3 network represents a highly connected and active network *in vitro*.

hDGs Form Synaptic Connections with hCA3s

Next, we tested whether hDG and hCA3 formed synaptic connections *in vitro*. We utilized microfluidic devices, a two-compartment system connected by narrow grooves, which allows axonal growth but restricts neuronal migration (Figures 6A and S5A). We seeded 3-week-old hDGs and hCA3s (labeled LV-Grik4-G-GFP) into the 2 compartments of the device (Figure 6C). 3- to 4-week-old co-cultures were incubated with the rabies virus (Figure 6C), which traced all the presynaptic neurons that monosynaptically connected to hCA3 neurons (Figure 6C, right). We observed RFP^+ presynaptic cells in the hDG compartment as well as in the hCA3 compartment. The presence of RFP^+ hDG suggested that microfluidic device-based reconstruction of the DG-CA3 circuit *in vitro* could mimic the synaptic connections between 2 spatially separated cell populations in the absence of afferent activity and exogenous axon guidance cues.

We also tested whether hDGs and hCA3s could connect in a co-culture. A co-culture system would eschew the need for the microfluidic device and would facilitate the study using multiple cell lines. Transmission electron microscopic analysis of the co-culture containing

hDG and hCA3 (ratio 1:1) revealed numerous synaptic vesicles (Figures S5B and S5C, red arrowheads) adjacent to electron-dense postsynaptic densities (PSDs) on neuronal processes (Figures S5B and S5C, red arrows), suggesting the presence of neuronal synapses in the co-culture. Next, we used the rabies-tracing assay by labeling postsynaptic hCA3s with the LV-Grik4-G-GFP reporter to test direct synaptic connections between hDG and hCA3s. We dissociated hDG and hCA3s into single-cell suspensions (at 3 WIV), followed by mixing them at a 1:1 ratio and co-culturing them together for 3 weeks. When the co-culture was infected with ΔG-RV (red), we observed postsynaptic (GFP^+RFP^+), presynaptic (GFP^-RFP^+), and rabies-uninfected populations in the culture (Figure 6D). Immunostaining for CALB1 (Brandt et al., 2003) indicated that a subset of presynaptic neurons was indeed $CALB1^+$ hDGs (Figure 6E) that made synaptic contacts with $Grik4^+$ hCA3 subtypes.

hCA3 Show Reduced Spontaneous Activity in a Cohort of SZ

Next, we applied the hDG-hCA3 co-culture to model SZ-associated neuronal connectivity defects in the hippocampus. SZ is a polygenic and heterogeneous disorder, and affected brain regions include the prefrontal cortex, basal ganglia, and limbic system, including the thalamus, hypothalamus, amygdala, and hippocampus. Declarative memory, a hippocampus-dependent function, is a key area of impairment in SZ (Cirillo and Seidman, 2003; Rasetti et al., 2014). Postmortem studies have indicated a reduced level of glutamate transmission in the MF pathway in SZ (Kolomeets, 2007; Kolomeets et al., 2007; Li et al., 2015; Tamminga et al., 2010; Tamminga and Zukin, 2015). In addition, mouse studies have also implicated the MF pathway and other hippocampal networks in SZ. For example, immature DG phenotype has been linked with abnormal behavior related to SZ (Guo et al., 2013; Hagihara et al., 2014; Ohira et al., 2013; Walton et al., 2012). A mouse model of SZ with disruptions in 22q11.2 reported altered calcium kinetics in CA3 (Earls et al., 2010). Our previous work based on analyses of the differentiated neurons of SZ and healthy iPSCs has revealed that differentiation and spontaneous activity of DG neurons was significantly reduced in SZ cohort (Yu et al., 2014). Additionally, decreased synaptic maturation, decreased neuronal connectivity, and aberrant neurotransmitter secretion from SZ neurons have also been reported (Brennand and Gage, 2011; Hook et al., 2014). The full characterization of the hippocampal pathologies, in this cohort, has not been explored, and it is still unclear how hippocampal dysfunction might correlate with SZ (Tamminga et al., 2010). To address this, we generated hpNPCs from iPSCs from SZ patients and healthy individuals characterized in previous studies (Brennand et al., 2011; Yu et al., 2014) using the differentiation protocol explained in Figure 1 (Figures 7A, 7B, S6, and S7A).

There were no differences in ELAVL2 and SCGN subtypes between SZ hCA3s and healthy hCA3s at 6 WIV, indicating no disparate developmental propensity (Figures 7A, 7B, S6, S7A, and S7B). To investigate the functional activity of the iPSC-derived hDG-hCA3 circuits, we differentiated hDGs and hCA3s for 3 weeks separately and then dissociated and co-cultured them together in a 1:1 ratio. We allowed the co-culture to grow on MEA plates (Figure S7C). 3 weeks after replating, we observed a decrease in the number of spontaneous spike and network bursts in SZ-derived hDG-hCA3 co-cultures (Figures 7E and S7D). We explored whether this decrease resulted from a loss of interneurons in hCA3 population, as has been reported in the hippocampus and prefrontal cortex in mouse models of SZ (Lewis

et al., 2012; Nakazawa et al., 2012). Immunostaining analysis with GABA showed that healthy and SZ groups produced a similar number of interneurons, with low occurrence (<5%) in both groups (Figures S7E and S7F), suggesting that the reduction in spontaneous activity might not be based on the number of interneurons present in the population. While this finding does not rule out the possibility of interneuron dysfunction in SZ, our study suggests that the reduction in activity might result from the reduced activity in DG neurons and/or synaptic input on CA3 neurons and a reduction in CA3 activity.

Next, we tested both healthy and SZ hCA3s for the spontaneous neural network activity. *In vitro* MEA recording of iPSC-hCA3 culture at 6 WIV revealed a significant reduction in the number of spikes in SZ hCA3 compared to healthy controls (Figure 7C), indicating attenuation in neural network activity within the hCA3s derived from SZ patients. Furthermore, significant reductions in network properties such as network bursts, spike per network burst, and synchronicity were also observed in SZ hCA3s (Figures 7C and S7G). However, younger SZ-hCA3s showed activity (spikes) at an early stage of development (1–5 WIV) that was similar the healthy group (Figure S7H). There was no difference in the total number of neural cells between healthy and SZ hCA3s (Figure S7B).

Next, we performed whole-cell patch-clamp recordings to measure the excitability of hCA3s derived from SZ patients. We selected neurons labeled by LV-Elavl2-EGFP reporter (at 4 WIV) for recording (Figures 7A and 7B). Similar to healthy hCA3s, SZ hCA3s showed equivalent levels of Na^+ and K^+ currents (Figure S7J). However, SZ hCA3s revealed reductions in the total and the maximum number of evoked APs in response to somatic injection of depolarizing current steps (Figures 7D and S7K). Also, input conductance (nS) was significantly higher in SZ hCA3s ($p = 0.004$). While it remains to be determined how this alteration results in the etiologies in the adult patient brain (Li et al., 2015), it suggests that activity deficits in a gluta-matergic pyramidal neuron population during development might play a role in SZ pathology.

DISCUSSION

Uncovering the mechanisms of the development and functioning of human neural connections has important applications in fundamental and clinical research. However, this research has remained challenging due to a lack of accessibility to human brain material and *in vitro* models of lineage-specific connection. In this study, we report directed differentiation of several hippocampal pyramidal neuronal subtypes and present a model to study connectivity between two cell classes.

We showed that the hpNPCs are enriched with medial pallium markers that give rise to the hippocampus. In a chemically defined medium with the addition of Wnt3a, hpNPCs differentiated to DG and CA3 neurons, mimicking *in vivo* hippocampal development. Wnts and other morphogens are known to play a role in shaping cell-fate specificity in a concentration-dependent manner (Liu and Zhang, 2011). While it remains to be determined by which mechanism the DG and CA3 acquire such a specific regional identity, one possibility could be dose-dependent differential regulation of Prox1, because Wnt3a directly regulates Prox1 expression (Karalay et al., 2011).

An important feature of our differentiation approach is the efficient patterning whereby neurons of distinct molecular identities are generated, preserving the molecularly heterogeneous nature of the *in vivo* human hippocampus. Notably, the pyramidal neurons generated here *in vitro* illustrated the enrichment of >20 CA3 genes in the hCA3 population, recapitulating a comprehensive patterning, ranging from abundant to rare subtypes including genes that are expressed by a subpopulation of CA3 neurons. Differentiation from iPSCs also followed similar cell-fate patterning. The CA3 gene list is based on published reports of gene expression in mouse CA3, so we cannot preclude the possibility that the hCA3 population might represent more CA3 subtypes. The genes expressed in the green cluster, in the hCA3 single-cell transcriptome data, may reflect the presence of more subtypes, including those uniquely expressed in human. Individual CA3 cells can project broadly (Amaral and Witter, 1989; Ishizuka et al., 1990; Ropireddy and Ascoli, 2011). Variability in gene expression is known to correlate with differences in protein expression, electrophysiological properties, and network connectivity (Cembrowski et al., 2016; Dong et al., 2009). The molecular heterogeneity within the hCA3 may represent *in vivo* subtypes underlying higher-order functional parcellations.

While subtype heterogeneity is known to exist in the hippocampus, we have made an unexpected discovery of a human CA3 subtype that is absent in mouse. The hippocampus is a significant target for intervention in brain disorders; animal models can only reproduce the conserved structural attributes and vulnerabilities. The unique advantage of hCA3s is the recapitulation of human CA3 differentiation, which future studies should utilize to probe human gene function and novel therapeutics.

Modeling neuropsychiatric disorders using hiPSCs holds great promise for revealing the diseases' etiologies and identifying potential targets for drug discovery. However, an impediment to using hiPSCs is the difficulty of developing models that include relevant neuronal subtypes and functions. Neuronal monolayers have proven to be robust in representing a relatively homogeneous population of a single neuronal subtype while lacking complexities seen *in vivo* (e.g., network activity). Threedimensional organoids, in contrast, constitute several neuronal subtypes and are potentially self-organized to form networks (Lancaster et al., 2013). However, this spontaneous selforganization causes variability between different brain regions (Eiraku and Sasai, 2011; Lancaster et al., 2013) and between different batches of cells (Lancaster and Knoblich, 2014).

In this study, co-culturing the postsynaptic CA3 pyramidal neuron with presynaptic DG neurons allowed us to explore the connectivity between these neurons. The directed differentiation of DG and CA3 classes ensures better recapitulation of multiple subtypes and class lineages. Furthermore, in the neuronal co-culture, the spontaneous neuronal connections appear to form reliably. This neuronal pair model exhibits adequate complexities reproducibly and parallels *in vivo* neuronal pathways. For example, the neurons projecting long axons (>300 μm in length) through the microfluidic device recapitulate the communication between the DG and CA3 areas (Figure 6C), mimicking essential aspects of intrinsically patterned connectivity between these two brain regions.

hCA3s Reveal Hippocampal Activity Deficits in a Cohort of SZ

Copious studies have implicated diminished neuronal communication in many neuropsychiatric disorders. Studying patient-derived human neurons *in vitro* is proving to be a reasonable approach for modeling such disorders (Avior et al., 2016). In this study, we explored the neurodevelopmental aspects of SZ, focusing on differentiating neurons from NPCs, and we uncovered an alteration in activity in SZ-hCA3s in our cohort. By modeling a lineage-specific hippocampal circuit, we also detected a patient-specific decrease in intrinsic neuronal activity. Our study supports the previous findings of potential disruptions in the early brain development of SZ patients in this cohort. Future longitudinal studies with bigger sample sizes are warranted to demonstrate that these cellular phenotypes causally relates to SZ etiology. The hippocampal co-cultures used here are scalable and can be suitable for cohorts with a sizable number of patients.

In summary, these results highlight the power of directed differentiation of hESCs/iPSCs to characterize human neuronal subtypes and model intrinsic connectivity. More broadly, our findings also emphasize the network relevance of hESC/iPSC-based disease modeling, an essential target for diagnosis and medication. This work points the way toward future disease modeling efforts, centered on neural networks, for efficient drug screening and treatments for psychiatric and neurological disorders.

STAR★METHODS

Detailed methods are provided in the online version of this paper and include the following:

CONTACT FOR REAGENT AND RESOURCE SHARING

Further information and requests for resources and reagents should be directed to and will be fulfilled by the Lead Contact, Fred H. Gage (gage@salk.edu).

EXPERIMENTAL MODEL AND SUBJECT DETAILS

All the ESC studies are done using HUES6 obtained from HSCI iPS Core. The iPS cells were obtained from the Coriell Institute Cell Repository. Protocols were previously approved by the Salk Institute Institutional Review Board and informed consent was obtained from all subjects.

For iPS cell derivation, patients were originally selected based on the high likelihood of a genetic component to disease (Brennand et al., 2011). Patient 1 (GM01792, male, 26 years of age, Jewish Caucasian) displayed episodes of agitation, delusions of persecution, and fear of assassination. Patient 2 (GM01835, female, 27 years of age, Jewish Caucasian) had a history of schizoaffective disorder and drug abuse. Her brother, patient 3 (GM02038, male, 22 years of age, Caucasian) was diagnosed with SZ at six years of age and committed suicide at 22 years of age. Patient 4 (GM02497, male, 23 years of age, Jewish Caucasian) was diagnosed with SZ at age 15 and showed symptoms including paralogical thinking, affective shielding, splitting of affect from content, and suspiciousness. Apparently healthy individuals with normal psychiatric evaluations were included as healthy controls. GM02937 (male, 22 years of age), GM03651 (female, 25 years of age), GM04506 (female, 22 years of

age), WT33 (female, 51 years of age). For iPS differentiation to hippocampal neurons, 2 lines derived per individual were used. For the neuronal activity assays by MEA and whole cell patch clamp recordings only one line per individual has been studied.

Human postmortem brain samples were obtained from the brain bank of the Shiley-Marcos Alzheimer's Disease Research Center (ADRC) at the University of California, San Diego (UCSD) and the San Diego County Medical Examiner's Office. Briefly, the extracted brain was sectioned coronally and a tissue block containing the hippocampus was placed in 2% paraformaldehyde for subsequent sectioning by microtome. After 24 hours of fixation, the tissue was transferred to a 30% sucrose solution for cryoprotection and was then sectioned 48-72 hours later. Sections (40 μm thick) were stored in cryoprotective medium at −20°C for subsequent immunochemical studies.

Mice—All experimental procedures were approved by the Institutional Animal Care and Use Committee at The Salk Institute for Biological Studies. For immunohistochemistry, 3-6 months old wild-type C57BL6 (strain: C57BL/6NHsd) mice were used. They were housed in standard housing with no more than 5 animals per cage.

For *in vivo* transplantation experiment, NOD-SCID (NOD.CB17-Prkdc^{scid}/NCrHsd) mice (Envigo) were housed in sterile housings with 2-3 animals per cage. 2 months old adult NOD/SCID mice were subjected to *in vivo* transplantation experiment. Both male and female mice were used for immunohistochemistry and *in vivo* cell transplantation.

METHOD DETAILS

Cell culture—HuES6 and hiPSC colonies were kept in feeder-free conditions in mTeSR1 medium (Stem Cells Technologies) and passed using Colla-genase IV (Life Science, 1 mg/ml). HuES6 and hiPSC colonies were dissociated with Collagenase IV and plated onto low-adherence dishes in mTeSR^{1} medium with the addition of Rock inhibitor (Enzo Life Sciences, 10 μM) to generate floating embryoid bodies (EBs).

To obtain pan NPCs, the following day the EBs were treated with Noggin (0.5 μg/ml) in Dulbecco's modified Eagle's medium (DMEM)/F12 (Invitrogen) plus N2 and B27 supplements (Invitrogen). The treatment was continued for 7 days followed by plating onto polyornithine/laminin (Sigma)-coated dishes in DMEM/F12 plus N2 and B27 supplements (N2B27 medium) and laminin (Invitrogen, 1 μg/ml) to facilitate the attachment of the EBs. Within a few days, rosettes were manually collected and dissociated with Accutase (Chemicon) and plated onto polyornithine/laminin-coated dishes with NPC media (DMEM/F12, N2, B27, and 20 ng/ml FGF2).

To obtain hpNPCs, EBs were treated with DKK1 (0.5 μg/ml), SB431542 (10 μM), Noggin (0.5 μg/ml) and cyclopamine (1 μM) in Dulbecco's modified Eagle's medium (DMEM)/F12 (Invitrogen) plus N2 and B27 supplements (Invitrogen) as described previously (Yu et al., 2014). The treatment was continued for 20 days followed by plating onto polyornithine/laminin (Sigma)-coated dishes in DMEM/F12 plus N2 and B27 supplements (N2B27 medium) and laminin (Invitrogen, 1 μg/ml) to facilitate the attachment of the EBs. Within a few days, rosettes were manually collected and dissociated with Accutase (Chemicon) and

plated onto polyornithine/laminin-coated dishes with NPC media (DMEM/F12, N2, B27, and 20 ng/ml FGF2).

To obtain mature hCA3s, NPCs were plated into polyornithine/laminin-coated plates in N2B27 medium in the presence of ascorbic acid (Sigma, 200 nM), cAMP (Fisher Scientific, 500 μg /ml), BDNF (20 ng/ml), laminin (1 μg/ml) and Wnt3a (R&D Systems, 5 ng/ml). Wnt3a was removed after 3 weeks and the differentiation was continued for a few more weeks.

hDG neurons were derived by using ascorbic acid (Sigma, 200 nM), cAMP (Fisher Scientific, 500 μg /ml), BDNF (20 ng/ml), laminin (1 μg/ml) and Wnt3a (R&D Systems, 20 ng/ml) as previously described (Yu et al., 2014).

SZ and control hiPSCs were derived and characterized as previously described (Brennand et al., 2011).

Immunocytochemistry—Cells were fixed in 4% paraformaldehyde for 15 minutes. Cells were subsequently blocked and permeabilized in PBS containing 0.1%–0.2% Triton X-100 and 10% horse serum. Coverslips were incubated with primary antibody in blocking solution overnight at 4°C, washed in Tris-buffered saline, incubated with secondary antibodies for 30 minutes at room temperature (RT), counterstained with DAPI, washed, mounted on slides using PVA-DABCO (Sigma-Aldrich), and dried overnight protected from light. Fluorescent signals were detected using a Zeiss 710 confocal microscope and images were processed with ImageJ. Composite images of microfluidic device (Figure 6B and 6C) were obtained by stiching multiple consecutive images with overlapping areas to show axons. Cells were traced using Neurolucida (MBF Bioscience) for branched structure analysis.

Immunohistochemistry—Immunohistochemistry of mouse brain sections was performed as previously described (Subramanian et al., 2011). Briefly, mouse tissues were permeabilized with 0.3% Triton X-100 in PBS followed by blocking in PBS containing 0.2% Triton X-100 and 10% horse serum. Floating sections were incubated with primary antibody in blocking solution overnight at 4 °C on a shaker, washed in Tris-buffered saline, incubated with secondary antibodies for 2 hours at room temperature (RT), counterstained with DAPI, washed, mounted on slides, coverslipped using PVA-DABCO (Sigma-Aldrich), and dried overnight protected from light.

The following antibodies and dilutions were used: GFP (1:500) Map2ab (1:1000), Elavl2 (1:250), Elavl2/4 (1:500), Lhx9 (1:50), Nestin (1:200), Scgn (1:250, Invitrogen), NeuN (mouse, 1:100, Millipore), Prkcd (1:100), Grik4 (1:100), OTX (1:100), GABA (1:1000), CTIP2 (1:500), and Vglut1 (1:500).

Fluorescence signals were detected using a Zeiss 710 confocal microscope and images were processed with Zen and ImageJ/Fiji (https://imagej.nih.gov/ij/). For larger tissue areas, such as human hippocampus, composite of multiple consecutive images with overlapping areas were shown (Figure 4F, Figure S2H).

Sectioning of mouse brain tissue for immunohistochemistry: Both C57BL6 and NOD-SCID mice were anesthetized with ketamine/xylazine and perfused transcardially with 0.9% saline followed by 4% paraformaldehyde. The brain samples were postfixed with 4% paraformaldehyde and equilibrated in 30% sucrose. Coronal sections of 40-50 μm were prepared with a sliding microtome. Brain sections of one-in-four to one-in-six series were selected for immunostaining.

RNA extraction, qRT-PCR, RNA-seq—Total cellular RNA was extracted from 3-5×10^6 cells using the RNA-BEE (QIAGEN), according to the manufacturer's instructions, and reverse transcribed using the high-capacity cDNA synthesis kit from AB Biosystems. qPCR was done using SYBR green (Life Technologies). qPCR results were analyzed using SDS Software v 3.2 for 7900HT real-time PCR system.

Poly(A)$^+$ RNA-seq analysis—Poly(A)$^+$ RNA was selected and fragmented to prepare sequencing libraries using the Illumina TruSeq Stranded RNA sample preparation kit. Libraries were sequenced using an Illumina HiSeq 2500 sequencer at the Next Generation Sequencing (NGS) core at the Salk Institute according to manufacturer's instructions. Libraries were sequenced at single- end 50-bp reads at an average depth of 10 million reads per library. Adaptors and low-quality sequence ends were trimmed using cutadapt (v.1.3). Sequencing reads from all libraries were mapped to rat (rn5) genome using STAR (v.2.3.1o). Read counts mapping to UCSC RefSeq gene annotations were obtained using htseq-count (v.0.5.4) (Anders et al., 2015). Differential expression analysis between groups of samples was performed with DESeq (v.1.16.0), using a false discovery rate cutoff of 5%.

Single cell RNA-seq

Sample preparation, encapsulation: huES6-derived NPCs were differentiated to hCA3 for 14DIV. Differentiating hCA3 population were dissociated into a single cell suspension by enzymatic dissociation by treating with Accutase (Stem cell technologies). Cells were collected in PBS containing 0.1%BSA on ice. The cell suspension obtained was filtered with 22-μm filter (Millipore) and kept in cold PBS-BSA solution. Before counting, trypan blue was added to the cell suspension and the viability, cell density and presence of clumps were assayed on a TC20 Automated Cell Counter. Cell suspensions at a final dilution of 2,500 cells/μL and containing no less than 85% live cells were taken for the encapsulation and later steps. All reagents for encapsulation, cDNA synthesis, library preparation and sequencing were from Illumina Inc. Cell suspensions were loaded into a ddSEQ cartridge in a ratio of 21.5 μL Cell enzyme mix to every 4.5 μL cell suspension. 60 ul of 3′ barcode suspension mix and encapsulation oil were also loaded on the cartridge. The chip was then processed on a ddSEQ Single-Cell Isolator for about 5 minutes to generate single cell droplets.

Reverse transcription and cDNA synthesis: Encapsulated samples were transferred to a 96- well plate and reverse transcription mix was added and followed by reverse transcription on a thermal cycler. When the reverse transcription was done, droplet disruptor was added to the product. This was followed by the first strand purification using magnetic beads. The beads were immobilized using magnetic peg stand and dynamag and supernatant was discarded. The beads were washed twice with 80% EtOH. 30 uls of resuspension buffer was

added for elution and supernatant was transferred to a new tube. The purified first strand was used to synthesize the second strand to generate the double strand cDNA. The cDNA was purified again using magnetic beads, followed by 80% EtOH wash and elution.

Tagmentation: Amplified cDNA was simultaneously fragmented and barcoded by tagmentation using Tagment enzyme on thermal cycler. DNA adapters were added for cluster formation. Followed by the index addition, libraries were cleaned up using magnetic beads as before. Purified libraries were eluted with 20 ul resuspension buffer. 1 ul of eluted product was assessed on an Agilent BioAnalyzer. Library size was about 500bp. Libraries were sequenced using an Illumina HiSeq 2500 sequencer at Illumina Inc. (San Diego, CA) using sure-cell-sequencing primers.

Analysis of single cell transcriptome: Raw data were processed using custom scripts and code for demultiplexing the reads, extracting unique molecular identifiers (UMIs), and assigning reads to cells with distinct cellular barcodes. Reads that had missing pairs and cells with barcodes that could not be assigned to known barcode combinations (allowing for correction of barcodes with only one error) were filtered from downstream analysis. Reads assigned to each cell were mapped to the human genome (hg19) using the STAR splice-aware aligner (Dobin et al., 2013) and duplicated reads with the same UMI aligning to the same genomic position were filtered to minimize amplification bias. Raw gene counts were obtained using the HOMER analysis pipeline (Heinz et al., 2010) using the most abundant isoform as proxy for gene expression. The script will be available upon request.

Preparation of microfluidic device: We designed a microfluidic device consisting of two separate compartments connected by 400-um long × 3-um wide microgrooves. Microfluidic devices were generated as published (Kim et al., 2012). Devices were coated with 0.5 mg/ml poly-L-lysine (PLL, MW 70,000–150,000, Sigma) overnight, washed three times with DI water, and air-dried. After assembling devices on these plates, all reservoirs and channels of the devices were coated with polyornithine/laminin (Sigma).

Multielectrode array recording: Neuronal networks derived from hESCs and hiPSCs were plated on polyornithine/laminin (Sigma)-coated plates embedded with MEAs (Axion Biosystems). Cell cultures were recorded at 37°C with a temperature controlled chamber with 5% CO2 for 10 min. Plate activity was recorded with the Maestro system in conjunction with the Axion's Integrated Studio (AxIS) software configured to Neural: Broadband. The threshold for spike detection was set to 5.5 or 6 standard deviation. Spikes files were processed and analyzed with NeuralMetric Tool (Axion Biosystems). Spike rate is calculated from total number of spike per second. Spike rate normalized to number of active electrode is represented as mean spike rate (Hz).

All the iPS derived hCA3 culture or hDG+hCA3 co-cultures were differentiated parallel. Followed by dissociating and replating on multi electrode well plates (for simultaneous recordings) and on control plates (for immunohistochemistry) at 3 weeks *in vitro*. Maintaining healthy neurons for weeks is challenging and some cultures invariably fail or become contaminated. Moreover, dissociation of 3 weeks old neurons causes decreased neuronal survival in culture. When a neural culture failed (e.g., cell death, contamination) in

the control plate, the experiments were abandoned as all assays (including MEA) were conducted on neurons cultured in parallel. If, however, at least three neural cultures from both healthy and SZ genetic background remained, analysis was completed.

Electrophysiology: Recordings were performed from cells at 6 weeks of differentiation on acid-etched coverslips labeled with Grik4-GFP. Individual coverslips were transferred into a heated recording chamber and continuously perfused (1 ml per minute) with artificial cerebrospinal fluid bubbled with a mixture of CO_2 (5%) and O_2 (95%) and maintained at 25 °C. Artificial cerebrospinal fluid contained (in mM) 121 NaCl, 4.2 KCl, 1.1 $CaCl_2$, 1 $MgSO_4$, 29 $NaHCO_3$, 0.45 NaH_2PO_4-H_2O, 0.5 Na_2HPO_4 and 20 glucose (all chemicals from Sigma-Aldrich). For whole-cell recordings, a 40 × water-immersion objective, differential interference contrast filters (all from Olympus, Waltham, MA, USA), an infrared digital camera (Rolera XR-Qimaging, Surrey, BC, Canada), a digidata 1440A/Multiclamp 700B and Clampex 10.3 (Molecular Devices, Sunnyvale, CA, USA) were used. Patch electrodes were filled with internal solutions containing 130 mm K-gluconate, 6 mm KCl, 4 mm NaCl, 10 mm Na-HEPES, 0.2 mm K-EGTA; 0.3 mm GTP, 2 mmMg-ATP, 0.2 mm cAMP, 10 mm d-glucose, 0.15% biocytin and 0.06% rhodamine. The pH and osmolarity of the internal solution were close to physiological conditions (pH 7.3, 290–300 mOsmol). Data were all corrected for liquid junction potentials (10 mV). The resistance of the patch electrodes was around 5 MOhm. Electrode capacitances were compensated online in cell-attached mode (~7 pF). Recordings were low-pass filtered at 2 kHz, digitized and sampled at intervals of 50 ms (20 kHz). To control the quality and the stability of the recordings throughout the experiments, access resistance, capacitance and membrane resistance were continuously monitored online and recorded. The access resistance of the cells in our sample was ~48 MOhm.

For electrophysiology data (Figure 7E) total number of evoked APs were measured in 35 depolarization steps and maximum number of evoked APs (**p = 0.008) were recorded over 400 ms recordings.

Ex vivo brain slice electrophysiology: Three months post transplantation surgery, mice (5 months old) were anesthetized with ketamine/xylazine and transcardially perfused with ice cold, bubbling (95% O2/5% CO2) NMDG cutting solution [consisting of (in mM): NMDG 105, HCl 105, KCl 2.5, NaH2PO4 1.2, NaHCO3 26, Glucose 25, Sodium L-Ascorbate 5, Sodium Pyruvate 3, Thiourea 2, MgSO4 10, CaCl2 0.5, 300mOsm, pH = 7.4]. The brain is blocked coronally with a brain matrix (Zivic Instruments; Pittsburg, PA) and acute coronal slices (300μm) were cut on a vibratome (VT1000S, Leica Microsystems; Buffalo Grove, IL) through the dorsal hippocampus in ice cold, bubbling NMDG based cutting solution. Slices were allowed to recover for 15 minutes at 32°C in bubbling NMDG cutting solution. Slices were then transferred to a holding chamber consisting of normal ACSF [consisting of (in mM): NaCl 125, KCl 2.5, NaH2PO4 1.25, NaHCO3 25, D-Glucose 12.5, MgCl2 1, CaCl2 2, pH = 7.4, 295 mOsm] at 28° C. After at least one hour of recovery the slices were placed in a chamber and aCSF was perfused over the slices at ~2mL/min. CA3 pyramidal cells were visually identified under IR- DIC optics (Ziess Axioskop2; Oberkocken, Germany) at 40x and hCA3 neurons were confirmed to express eGFP with brief confirmation in the

epifluorescent channel. Voltage clamp or current clamp (33°C) recordings were made from the CA3 region of dorsal hippocampus (~−1.8mm bregma). 4-5 MΩ patch pipettes (WPI; Sarasota, FL) were pulled from borosilicate glass on a P-97 pipette puller (Sutter Instruments; Novato, CA) and filled with internal solution consisting of (in mM): KMeSO4 135, KCl 5, CaCl2 0.5, HEPES 5, EGTA 5, Mg-ATP 2, Na-GTP 0.3, pH = 7.3, 305 mOsm. Series resistance (< 30MOhms) was initially compensated and monitored continuously throughout the experiment and the data were rejected if the parameters changed by more than 20% over the duration of the recording. Voltage-clamp recordings were performed using a Multiclamp 700A (Molecular Devices; Sunnyvale, CA), digitized (Digidata 1440; Molecular Devices; Sunnyvale, CA) at 10 kHz and filtered at 2 kHz. Current clamp recordings were filtered and digitized at 10 kHz and collected with pClamp 9 (Molecular Devices; Sunnyvale, CA). Data were analyzed with Clampfit 9 and custom MATLAB scripts.

For whole-cell current clamp studies, resting membrane potential (Vrest) was measured immediately following break-in. Current-voltage (IV) curves were plotted from 750 ms current steps from −350pA in +50pA steps every 20 s. Measurement of steady state currents were used to plot the IV curve. The average of 10 current ramps (0.05Hz) to 1nA over 500 ms was used to determine rheo-base current (or current injection value sufficient to elicit first AP), AP threshold and latency to first AP. AP threshold was calculated as the point where the first derivative of the upstroke phase of the AP equals 20mV/ms. AP amplitude and half width were calculated in Clampfit 9.0 from current steps and averaged across all sweeps.

For voltage-clamp recordings, all experiments were initially held at −60mV. Voltage steps (500 ms) from −120mV to +20mV were given in 20mV steps every 20 s. Measurements of steady state currents were used to plot voltage-current plots. Voltage ramps (over 500 ms) from −150 mV to +30 mV were also used to observe sodium spikes. Membrane properties (capacitance, membrane resistance and tau) were analyzed from the average of 10 sweeps using a −5mV step (20ms duration) at a holding potential of −60mV. At the end of recordings to isolate sEPSCs, cells were held at −70mV and 2 minute gap free recordings in the presence of 50 μM picrotoxin (MilliporeSigma, St. Louis, MO) was added to the bath to block fast GABAAR transmission. Frequency and amplitude measurements were made in template mode in Clampfit 9.0.

Rabies virus trans-neuronal tracing—Rabies virus trans-neuronal tracing was performed on 6WIV hiPSC or huES6 derived neurons transduced with LV-SYNP-HTG. For co-cultures LV-SYNP-HTG transduced postsynaptic culture was dissociated and replated with not infected presynaptic culture for at least 10days. Cultures were then transduced with Rabies-ENVADG-RFP After 10 days, hiPSC neurons were either dissociated with accutase for FACS analysis or fixed with 4% paraformaldehyde in PBS for fluorescent microscopy.

Electron microcopy—Cocultures were immersed in modified Karnovsky’s fixative (2.5% glutaraldehyde and 2% paraformaldehyde in 0.15 M sodium ca-codylate buffer, pH 7.4) for at least 4 hours, postfixed in 1% osmium tetroxide in 0.15 M cacodylate buffer for 1 hour and stained en bloc in 2% uranyl acetate for 1 hour. Samples were dehydrated in ethanol,

embedded in Durcupan epoxy resin (Sigma-Aldrich), sectioned at 50 to 60 nm on a Leica UCT ultramicrotome, and picked up on 300 mesh copper grids. Sections were stained with 2% uranyl acetate for 5 minutes and Sato's lead stain for 1 minute. Grids were viewed using a JEOL 1200EX II (JEOL, Peabody, MA) transmission electron microscope and photographed using a Gatan digital camera (Gatan, Pleasanton, CA), or viewed using a Tecnai G2 Spirit BioTWIN transmission electron microscope equipped with an Eagle 4k HS digital camera (FEI, Hilsboro, OR).

In vivo transplantation—All experimental procedures were approved by the Institutional Animal Care and Use Committee at The Salk Institute for Biological Studies. For transplantation, 3-week-old differentiating neurons infected with lentiviral vector carrying the Grik4-GFP reporter construct were dissociated and resuspended in PBS-glucose, ROCK inhibitor, BDNF, ascorbic acid, cAMP, and laminin at 2,000 cells per ul. Two-month-old NOD-SCID mice were anesthetized using ketamine/xylazine (100 mg/kg, 10 mg/kg) and 1 ul of cell suspension was delivered to the mouse hippocampus by stereotaxic surgery. The injection site was determined using the position of the lambda and bregma as reference as follows: anteroposterior, 1.5 mm; lateral, 2 mm; −2 mm (from dura). Then 5 months post-transplantation, animals were anesthetized with ketamine/ xylazine and perfused transcardially with 0.9% saline followed by 4% paraformaldehyde. The brain samples were postfixed with 4% paraformaldehyde and equilibrated in 30% sucrose. Coronal sections of 50 um were prepared with a sliding microtome. Brain sections containing the graft were selected for immunohistochemistry.

Plasmids—DNA sequences were amplified with Phusion High-Fidelity DNA Polymerase (NEB) using human genomic DNA (Promega) as a template and oligonucleotide primers adding restriction enzymes sites for standard cloning. The cloned DNA regions were fully sequenced. In the listed oligonucleotide sequence, the regions matching the genomic DNA are capitalized.

Construction of PROX1-5-TdTomato lentiviral reporter plasmid: PROX1-positive cells was tracked using a lentiviral reporter derived from a previously described PROX1-EGFP construct (Yu et al., 2014). In the new vector, (PROX1-5-EGFP) 598 bp (chr1:214,209,178-214,209,775 - UCSC Genome Browser on Human Feb. 2009 - GRCh37/hg19) of the human PROX1 3′UTR region, located immediately downstream of the gene stop codon, were introduced downstream to the EGFP stop codon.

Forward oligo to amplify human Prox1 3′UTR: 5′gggtgtacaagtaaAAATTTCAACAACTCTTTTTGAAT. It adds a BsrGI site.Reverse oligo to amplify human Prox1 3′UTR: 5′gcggtttaaacTTATTTTTCTTTTTTAATTTGGCC. It adds a PmeI site.

Construction of GRIK4-EGFP lentiviral reporter plasmid: This was derived from a general pCSC-EGFP lentiviral vector introducing the human GRIK4 gene 5′ proximal region as promoter sequence. The 1,262 bp region (chr11:120,529,766-120,531,027 - UCSC Genome Browser on Human Feb. 2009 - GRCh37/hg19) is relative to the main validated gene

transcript (Human Gene GRIK4 uc009zax.1 - UCSC Genome Browser on Human Feb. 2009 - GRCh37/hg19) and includes the 50 bp transcript 5′UTR.

Forward oligo to amplify human GRIK4 1.3 kb promoter: G117: 5′cacatcgatATACTACTCTCCCAATCCAGGCACCT. It adds a ClaI site. Reverse oligo to amplify human GRIK4 1.3 kb promoter: 5′taaaccggtCTTCTATGAATCCTCATGGAGCCCC. It adds a AgeI site.

Construction of ELAVL2-EGFP lentiviral reporter plasmid: This was derived from the pCSC-SP-PW-GFP lentiviral vector introducing a composite DNA regulatory region consisting of two separate human genomic regions. First, the ELAVL2 gene 5′ proximal 1,212 bp relative to the transcript Human Gene ELAVL2 uc003zpu.3 (chr9:23,825,804-23,827,015 - UCSC Genome Browser on Human Feb. 2009 - GRCh37/hg19), which comprises the 260 bp transcript 5′ UTR, was cloned in the lentiviral vector upstream to the EGFP coding sequence. Next, a 1,059 bp enhancer (chr9:23,004,731-23,005,789 - UCSC Genome Browser on Human Feb. 2009 - GRCh37/hg19) corresponding precisely to the Element_643 of the Vista Enhancer Browser (Pennacchio et al., 2006), was introduced upstream of the above proximal promoter. This enhancer, located in the ELAVL2 3′ intergenic region is evolutionary conserved and has been experimentally validated in mouse. In the reporter vector the two described regions are linked by a NheI restriction site.

Forward oligo to amplify human ELAVL2 promoter. It adds a ClaI site followed by a NheI site (G175-5′tttaatcgatattgctagcGAAGTGAAAGCCAATTCAAACCGTGC).

Reverse oligo to amplify human ELAVL2 promoter from the 3′ end of first untranslated exon. It adds an AgeI site (G170-5′tggcaccggtCTTTCTCCCTTAAGGTTTTTGTGTAT).

Forward oligo to amplify human VISTA Enhancer 643. It adds a ClaI site (G176-5′tagtatcgatGACTGTGCCTGGTTAAAGGCTA). Reverse oligo to amplify human VISTA Enhancer 643. It adds a NheI site (G177-5′aagtgctagcGGGGATAGAATGAACCAAAAAC).

Construction of pCSC-GRIK4-LL-HTB plasmid: The vector is derived from lentiviral vector pBOB-synP-HTB, a gift from Edward Callaway & Liqun Luo (Addgene plasmid # 30195), replacing the synapsin promoter with the human GRIK4 and ELAVL2 promoter. First, the 1,262 bp Grik4 promoter and 1,212 ELAVL2-EGFP lentiviral reporter plasmid) was introduced into pBOB-synP-HTB, digested with ClaI and XbaI restriction enzymes to obtain pCSC-GRIK4-HTB (although ClaI and XbaI are double sites in pBOB-synP-HTB, in each case one site results conveniently blocked by Dam methylation). Next, to precisely restore the 5′UTR sequence present in the original pBOB-synP-HTB construct, a double strand XbaI-BmtI DNA cassette was cloned into pCSC-GRIK4-HTB.

Forward oligo to amplify GRIK4 promoter adds a ClaI site (G117-5′cacATCGATatactactctcccaatccaggcacct). Reverse oligo to amplify GRIK4 promoter. It adds a XbaI site (G134-5′caaTCTAGActtctatgaatcctcatggagcccc).

Top oligo for XbaI-BmtI cassette (G135-5′CTAGACGATAAGGGCGAATTCTGCAGATATCCATCACACTGGCGGCCGCTCGAGCATGCATCTAGAGGATCCGCTAG).

Bottom oligo for XbaI-BmtI cassette (G136-5′CGGATCCTCTAGATGCATGCTCGAGCGGCCGCCAGTGTGATGGATATCTGCAGAATTCGCCCTTATCGT).

Lentiviral preparation.: Briefly, lentivector plasmid and lentiviral packaging plasmids were introduced to 293 T human embryonic kidney cells using polyethyleneamine, and viral particles were concentrated by ultracentrifugation, aliquoted, titered and frozen for future use.

QUANTIFICATION AND STATISTICAL ANALYSES

All data values were presented as mean ± SEM. For parametric datasets with two groups, unpaired Student's t test (two way) was used to compare averages between two groups. For the non-parametric dataset with two groups, an unpaired two way Mann-Whitney test was performed. ANOVA analyses were used for comparisons of data with more than two groups. Post hoc group comparisons were performed with Bonferroni test and Sidak's multiple comparison test. For electrophysiology data (Figure 7E) two way t tests were performed using weighted mean and weighted standard deviation. A value of $p < 0.05$ was considered significant.

DATA AND SOFTWARE AVAILABILITY

The accession number for the raw sequencing data reported in this paper is GEO: GSE111979 (https://www.ncbi.nlm.nih.gov/projects/geo/query/acc.cgi?acc=GSE111979).

Supplementary Material

Refer to Web version on PubMed Central for supplementary material.

ACKNOWLEDGMENTS

We thank Illumina (San Diego, CA) and Bio-Rad (CA) for early access of SureCell WTA 3′ Library Prep Kit and the ddSEQ System. We thank Dr. Marilyn Farquhar for the use of the electron microscopy facility at the University of California, San Diego; Ying Jones, Jeffrey Chang, and Joan Valls for technical assistance; and Servier Medical Art and Jamie Simon for illustrations. We thank Mary Lynn Gage for editorial comments and Diana Yu and Ben Lacar for valuable comments on the project. This work was supported by CIRM (grant TG2-01158) (A.S.), the Streim Foundation (A.S.), the Helmsley Foundation (F.H.G.), the JPB Foundation (F.H.G.), the Engman Foundation (F.H.G.), the NIMH (grants U01-MH106882 and U19-MH106434) (F.H.G.), the NIMH (grants MH101634 and MH113924) (K.P.), a NARSAD Young Investigator Award (K.P.), the Razavi Newman Integrative Genomics and Bioinformatics Core Facility of the Salk Institute with funding from the NIH-NCI CCSG (grant P30 014195), and the Waitt Advanced Biophotonics Core Facility of the Salk Institute, with funding from the NIH-NCI CCSG (grant P30 014195) and NINDS (neuroscience core grant NS072031) and the Waitt Foundation.

REFERENCES

Abellán A, Desfilis E, and Medina L (2014). Combinatorial expression of Lef1, Lhx2, Lhx5, Lhx9, Lmo3, Lmo4, and Prox1 helps to identify comparable subdivisions in the developing hippocampal formation of mouse and chicken. Front. Neuroanat 8, 59. [PubMed: 25071464]

Akbarian S, Kim JJ, Potkin SG, Hagman JO, Tafazzoli A, Bunney WE, Jr., and Jones EG (1995). Geneexpression for glutamic acid decarboxylase is reduced without loss of neurons in prefrontal cortex of schizophrenics. Arch. Gen. Psychiatry 52, 258–266. [PubMed: 7702443]

Amaral DG, and Witter MP (1989). The three-dimensional organization of the hippocampal formation: a review of anatomical data. Neuroscience 31, 571–591. [PubMed: 2687721]

Amaral DG, Ishizuka N, and Claiborne B (1990). Neurons, numbers and the hippocampal network. Prog. Brain Res 83, 1–11.

Anders S, Pyl PT, and Huber W (2015). HTSeq–a Python framework to work with high-throughput sequencing data. Bioinformatics 31, 166–169. [PubMed: 25260700]

Arnold SE, and Trojanowski JQ (1996). Human fetal hippocampal development: II. The neuronal cytoskeleton. J. Comp. Neurol 367, 293–307. [PubMed: 8708011]

Avior Y, Sagi I, and Benvenisty N (2016). Pluripotent stem cells in disease modelling and drug discovery. Nat. Rev. Mol. Cell Biol 17, 170–182. [PubMed: 26818440]

Bertuzzi S, Porter FD, Pitts A, Kumar M, Agulnick A, Wassif C, and Westphal H (1999). Characterization of Lhx9, a novel LIM/homeobox gene expressed by the pioneer neurons in the mouse cerebral cortex. Mech. Dev 81, 193–198. [PubMed: 10330499]

Brandt MD, Jessberger S, Steiner B, Kronenberg G, Reuter K, Bick-Sander A, von der Behrens W, and Kempermann G (2003). Transient calretinin expression defines early postmitotic step of neuronal differentiation in adult hippocampal neurogenesis of mice. Mol. Cell. Neurosci 24, 603–613. [PubMed: 14664811]

Brennand KJ, and Gage FH (2011). Concise review: the promise of human induced pluripotent stem cell-based studies of schizophrenia. Stem Cells 29, 1915–1922. [PubMed: 22009633]

Brennand KJ, Simone A, Jou J, Gelboin-Burkhart C, Tran N, Sangar S, Li Y, Mu Y, Chen G, Yu D, et al. (2011). Modelling schizophrenia using human induced pluripotent stem cells. Nature 473, 221–225. [PubMed: 21490598]

Brennand K, Savas JN, Kim Y, Tran N, Simone A, Hashimoto-Torii K, Beaumont KG, Kim HJ, Topol A, Ladran I, et al. (2015). Phenotypic differences in hiPSC NPCs derived from patients with schizophrenia. Mol. Psychiatry 20, 361–368. [PubMed: 24686136]

Cembrowski MS, Wang L, Sugino K, Shields BC, and Spruston N (2016). Hipposeq: a comprehensive RNA-seq database of gene expression in hippocampal principal neurons. eLife 5, e14997. [PubMed: 27113915]

Cirillo MA, and Seidman LJ (2003). Verbal declarative memory dysfunction in schizophrenia: from clinical assessment to genetics and brain mechanisms. Neuropsychol. Rev 13, 43–77. [PubMed: 12887039]

Dobin A, Davis CA, Schlesinger F, Drenkow J, Zaleski C, Jha S, Batut P, Chaisson M, and Gingeras TR (2013). STAR: ultrafast universal RNA-seq aligner. Bioinformatics 29, 15–21. [PubMed: 23104886]

Dong HW, Swanson LW, Chen L, Fanselow MS, and Toga AW (2009). Genomic-anatomic evidence for distinct functional domains in hippocampal field CA1. Proc. Natl. Acad. Sci. USA 106, 11794–11799. [PubMed: 19561297]

Earls LR, Bayazitov IT, Fricke RG, Berry RB, Illingworth E, Mittleman G, and Zakharenko SS (2010). Dysregulation of presynaptic calcium and synaptic plasticity in a mouse model of 22q11 deletion syndrome. J. Neurosci 30, 15843–15855. [PubMed: 21106823]

Eiraku M, and Sasai Y (2011). Mouse embryonic stem cell culture for generation of three-dimensional retinal and cortical tissues. Nat. Protoc 7, 69–79. [PubMed: 22179593]

Galceran J, Miyashita-Lin EM, Devaney E, Rubenstein JL, and Grosschedl R (2000). Hippocampus development and generation of dentate gyrus granule cells is regulated by LEF1. Development 127, 469–482. [PubMed: 10631168]

Gothard KM, Hoffman KL, Battaglia FP, and McNaughton BL (2001). Dentate gyrus and ca1 ensemble activity during spatial reference frame shifts in the presence and absence of visual input. J. Neurosci 21, 7284–7292. [PubMed: 11549738]

Guo N, Yoshizaki K, Kimura R, Suto F, Yanagawa Y, and Osumi N (2013). A sensitive period for GABAergic interneurons in the dentate gyrus in modulating sensorimotor gating. J. Neurosci 33, 6691–6704. [PubMed: 23575865]

Hagihara H, Shoji H, Takao K, Walton NM, Matsumoto M, and Miyakawa T (2014). [Immaturity of brain as an endophenotype of neuropsychiatric disorders]. Nihon Shinkei Seishin Yakurigaku Zasshi 34, 67–79. [PubMed: 25076776]

Hashimoto T, Volk DW, Eggan SM, Mirnics K, Pierri JN, Sun Z, Sampson AR, and Lewis DA (2003). Gene expression deficits in a subclass of GABA neurons in the prefrontal cortex of subjects with schizophrenia. J. Neurosci 23, 6315–6326. [PubMed: 12867516]

He H, Mahnke AH, Doyle S, Fan N, Wang CC, Hall BJ, Tang YP, Inglis FM, Chen C, and Erickson JD (2012). Neurodevelopmental role for VGLUT2 in pyramidal neuron plasticity, dendritic refinement, and in spatial learning. J. Neurosci 32, 15886–15901. [PubMed: 23136427]

Heinz S, Benner C, Spann N, Bertolino E, Lin YC, Laslo P, Cheng JX, Murre C, Singh H, and Glass CK (2010). Simple combinations of lineagedetermining transcription factors prime cis-regulatory elements required for macrophage and B cell identities. Mol. Cell 38, 576–589. [PubMed: 20513432]

Hook V, Brennand KJ, Kim Y, Toneff T, Funkelstein L, Lee KC, Ziegler M, and Gage FH (2014). Human iPSC neurons display activity-dependent neurotransmitter secretion: aberrant catecholamine levels in schizophrenia neurons. Stem Cell Reports 3, 531–538. [PubMed: 25358781]

Ishizuka N, Weber J, and Amaral DG (1990). Organization of intrahippocampal projections originating from CA3 pyramidal cells in the rat. J. Comp. Neurol 295, 580–623. [PubMed: 2358523]

Iwano T, Masuda A, Kiyonari H, Enomoto H, and Matsuzaki F (2012). Prox1 postmitotically defines dentate gyrus cells by specifying granule cell identity over CA3 pyramidal cell fate in the hippocampus. Development 139, 3051–3062. [PubMed: 22791897]

Jung MW, and McNaughton BL (1993). Spatial selectivity of unit activity in the hippocampal granular layer. Hippocampus 3, 165–182.

Karalay O, Doberauer K, Vadodaria KC, Knobloch M, Berti L, Miquelajauregui A, Schwark M, Jagasia R, Taketo MM, Tarabykin V, et al. (2011). Prospero-related homeobox 1 gene (Prox1) is regulated by canonical Wnt signaling and has a stage-specific role in adult hippocampal neurogenesis. Proc. Natl. Acad. Sci. USA 108, 5807–5812. [PubMed: 21436036]

Kim HJ, Park JW, Byun JH, Vahidi B, Rhee SW, and Jeon NL (2012). Integrated microfluidics platforms for investigating injury and regeneration of CNS axons. Ann. Biomed. Eng 40, 1268–1276. [PubMed: 22302320]

Kimura J, Suda Y, Kurokawa D, Hossain ZM, Nakamura M, Takahashi M, Hara A, and Aizawa S (2005). Emx2 and Pax6 function in cooperation with Otx2 and Otx1 to develop caudal forebrain primordium that includes future archipallium. J. Neurosci 25, 5097–5108. [PubMed: 15917450]

Kohara K, Pignatelli M, Rivest AJ, Jung HY, Kitamura T, Suh J, Frank D, Kajikawa K, Mise N, Obata Y, et al. (2014). Cell type-specific genetic and optogenetic tools reveal hippocampal CA2 circuits. Nat. Neurosci 17, 269–279. [PubMed: 24336151]

Kolomeets NS (2007). The pathology of the hippocampus in schizophrenia. Zh. Nevrol. Psikhiatr. Im. S. S. Korsakova 107, 103–114. [PubMed: 18683339]

Kolomeets NS, Orlovskaya DD, and Uranova NA (2007). Decreased numerical density of CA3 hippocampal mossy fiber synapses in schizophrenia. Synapse 61, 615–621. [PubMed: 17476682]

Lancaster MA, and Knoblich JA (2014). Organogenesis in a dish: modeling development and disease using organoid technologies. Science 345, 1247125. [PubMed: 25035496]

Lancaster MA, Renner M, Martin CA, Wenzel D, Bicknell LS, Hurles ME, Homfray T, Penninger JM, Jackson AP, and Knoblich JA (2013). Cerebral organoids model human brain development and microcephaly. Nature 501, 373–379. [PubMed: 23995685]

Lee SM, Tole S, Grove E, and McMahon AP (2000). A local Wnt-3a signal is required for development of the mammalian hippocampus. Development 127, 457–467. [PubMed: 10631167]

Lewis DA, Curley AA, Glausier JR, and Volk DW (2012). Cortical parvalbumin interneurons and cognitive dysfunction in schizophrenia. Trends Neurosci. 35, 57–67. [PubMed: 22154068]

Li W, Ghose S, Gleason K, Begovic A, Perez J, Bartko J, Russo S, Wagner AD, Selemon L, and Tamminga CA (2015). Synaptic proteins in the hippocampus indicative of increased neuronal activity in CA3 in schizophrenia. Am. J. Psychiatry 172, 373–382. [PubMed: 25585032]

Liu H, and Zhang SC (2011). Specification of neuronal and glial subtypes from human pluripotent stem cells. Cell. Mol. Life Sci 68, 3995–4008. [PubMed: 21786144]

Marchetto MC, Carromeu C, Acab A, Yu D, Yeo GW, Mu Y, Chen G, Gage FH, and Muotri AR (2010).A model for neural development and treatment of Rett syndrome using human induced pluripotent stem cells. Cell 143, 527–539. [PubMed: 21074045]

Marchetto MC, Belinson H, Tian Y, Freitas BC, Fu C, Vadodaria KC, Beltrao-Braga PC, Trujillo CA, Mendes AP, Padmanabhan K, et al. (2016). Altered proliferation and networks in neural cells derived from idiopathic autistic individuals. Mol. Psychiatry 22, 820–835. [PubMed: 27378147]

Miller PD, Chung WW, Lagenaur CF, and DeKosky ST (1993). Regional distribution of neural cell adhesion molecule (N-CAM) and L1 in human and rodent hippocampus. J. Comp. Neurol 327, 341–349. [PubMed: 7680048]

Nakazawa K, Zsiros V, Jiang Z, Nakao K, Kolata S, Zhang S, and Belforte JE (2012). GABAergic interneuron origin of schizophrenia pathophysiology. Neuropharmacology 62, 1574–1583. [PubMed: 21277876]

Ohira K, Kobayashi K, Toyama K, Nakamura HK, Shoji H, Takao K, Takeuchi R, Yamaguchi S, Kataoka M, Otsuka S, et al. (2013). Synaptosomal-associated protein 25 mutation induces immaturity of the dentate granule cells of adult mice. Mol. Brain 6, 12. [PubMed: 23497716]

Pennacchio LA, Ahituv N, Moses AM, Prabhakar S, Nobrega MA, Shoukry M, Minovitsky S, Dubchak I, Holt A, Lewis KD, et al. (2006). In vivo enhancer analysis of human conserved non-coding sequences. Nature 444, 499–502. [PubMed: 17086198]

Rasetti R, Mattay VS, White MG, Sambataro F, Podell JE, Zoltick B, Chen Q, Berman KF, Callicott JH, and Weinberger DR (2014). Altered hippocampal-parahippocampal function during stimulus encoding: a potential indicator of genetic liability for schizophrenia. JAMA Psychiatry 71, 236–247. [PubMed: 24382711]

Robicsek O, Karry R, Petit I, Salman-Kesner N, Müller FJ, Klein E, Aberdam D, and Ben-Shachar D (2013). Abnormal neuronal differentiation and mitochondrial dysfunction in hair follicle-derived induced pluripotent stem cells of schizophrenia patients. Mol. Psychiatry 18, 1067–1076. [PubMed: 23732879]

Ropireddy D, and Ascoli GA (2011). Potential synaptic connectivity of different neurons onto pyramidal cells in a 3D reconstruction of the rat hippocampus. Front. Neuroinform 5, 5. [PubMed: 21779242]

Sakaguchi H, Kadoshima T, Soen M, Narii N, Ishida Y, Ohgushi M, Takahashi J, Eiraku M, and Sasai Y (2015). Generation of functional hippocampal neurons from self-organizing human embryonic stem cell-derived dorsomedial telencephalic tissue. Nat. Commun 6, 8896. [PubMed: 26573335]

Sarkar A, Marchetto MC, and Gage FH (2017). Synaptic activity: An emerging player in schizophrenia. Brain Res. 1656, 68–75. [PubMed: 26723567]

Shi TJ, Xiang Q, Zhang MD, Tortoriello G, Hammarberg H, Mulder J, Fried K, Wagner L, Josephson A, Uhlén M, et al. (2012). Secretagogin is expressed in sensory CGRP neurons and in spinal cord of mouse and complements other calcium-binding proteins, with a note on rat and human. Mol. Pain 8, 80. [PubMed: 23102406]

Small SA, Schobel SA, Buxton RB, Witter MP, and Barnes CA (2011). A pathophysiological framework of hippocampal dysfunction in ageing and disease. Nat. Rev. Neurosci 12, 585–601. [PubMed: 21897434]

Stranahan AM, Lee K, Becker KG, Zhang Y, Maudsley S, Martin B, Cutler RG, and Mattson MP (2010). Hippocampal gene expression patterns underlying the enhancement of memory by running in aged mice. Neurobiol. Aging 31, 1937–1949. [PubMed: 19070401]

Subramanian L, Sarkar A, Shetty AS, Muralidharan B, Padmanabhan H, Piper M, Monuki ES, Bach I, Gronostajski RM, Richards LJ, and Tole S (2011). Transcription factor Lhx2 is necessary and sufficient to suppress astrogliogenesis and promote neurogenesis in the developing hippocampus. Proc. Natl. Acad. Sci. USA 108, E265–E274. [PubMed: 21690374]

Tamminga CA, and Zukin RS (2015). Schizophrenia: evidence implicating hippocampal GluN2B protein and REST epigenetics in psychosis pathophysiology. Neuroscience 300, 233–242.

Tamminga CA, Stan AD, and Wagner AD (2010). The hippocampal formation in schizophrenia. Am. J. Psychiatry 167, 1178–1193. [PubMed: 20810471]

Thompson CL, Pathak SD, Jeromin A, Ng LL, MacPherson CR, Mortrud MT, Cusick A, Riley ZL, Sunkin SM, Bernard A, et al. (2008). Genomic anatomy of the hippocampus. Neuron 60, 1010–1021. [PubMed: 19109908]

Tripathi S, Pohl MO, Zhou Y, Rodriguez-Frandsen A, Wang G, Stein DA, Moulton HM, DeJesus P, Che J, Mulder LC, et al. (2015). Meta-and orthogonal integration of influenza ‘‘OMICs’’ data defines a role for UBR4 in virus budding. Cell Host Microbe 18, 723–735. [PubMed: 26651948]

Walton NM, Zhou Y, Kogan JH, Shin R, Webster M, Gross AK, Heusner CL, Chen Q, Miyake S, Tajinda K, et al. (2012). Detection of an immature dentate gyrus feature in human schizophrenia/bipolar patients. Transl. Psychiatry 2, e135. [PubMed: 22781168]

Wen Z, Nguyen HN, Guo Z, Lalli MA, Wang X, Su Y, Kim NS, Yoon KJ, Shin J, Zhang C, et al. (2014). Synaptic dysregulation in a human Ips cell model of mental disorders. Nature 515, 414–418. [PubMed: 25132547]

Williams ME, Wilke SA, Daggett A, Davis E, Otto S, Ravi D, Ripley B, Bushong EA, Ellisman MH, Klein G, and Ghosh A (2011). Cadherin-9 regulates synapse-specific differentiation in the developing hippocampus. Neuron 71, 640–655. [PubMed: 21867881]

Xu Q, Bernardo A, Walker D, Kanegawa T, Mahley RW, and Huang Y (2006). Profile and regulation of apolipoprotein E (ApoE) expression in the CNS in mice with targeting of green fluorescent protein gene to the ApoE locus. J. Neurosci 26, 4985–4994. [PubMed: 16687490]

Yu DX, Di Giorgio FP, Yao J, Marchetto MC, Brennand K, Wright R, Mei A, McHenry L, Lisuk D, Grasmick JM, et al. (2014). Modeling hippocampal neurogenesis using human pluripotent stem cells. Stem Cell Reports 2, 295–310. [PubMed: 24672753]

Zhao X, Lein ES, He A, Smith SC, Aston C, and Gage FH (2001). Transcriptional profiling reveals strict boundaries between hippocampal subregions. J. Comp. Neurol 441, 187–196. [PubMed: 11745644]

Highlights

- Differentiation of human CA3 pyramidal neuron is modeled using ESCs/iPSCs
- RNA-seq and immunocytochemistry revealed pyramidal neuron diversity
- Rabies virus tracing showed a connection between ESC-derived DG and CA3 neurons
- Schizophrenia hiPSC-derived DG-CA3 co-cultures present deficits in hippocampal activity

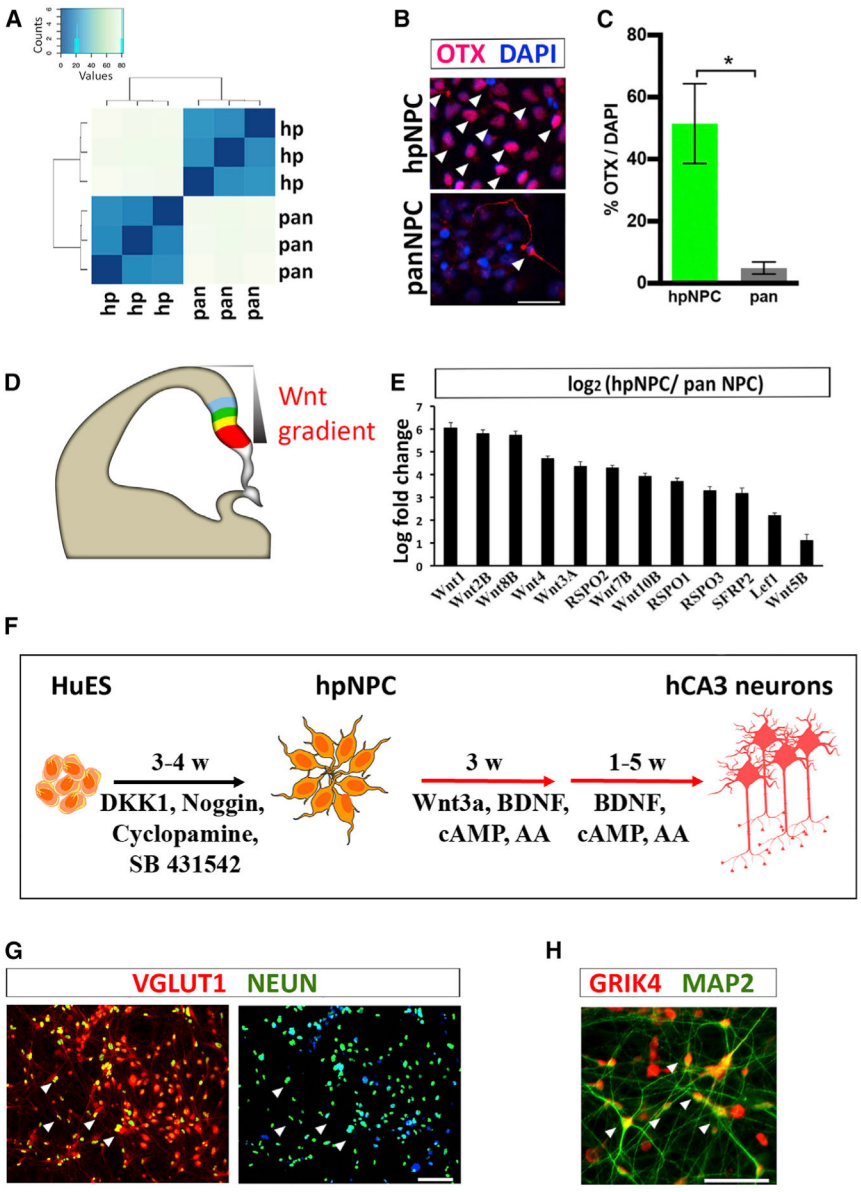

Figure 1. Generation of hCA3s from Human ESCs

(A) Hierarchical clustering based on differential transcriptomes between hpNPCs (hp) and panneuronal NPCs (pan).

(B and C) Immunostaining (B) and quantitation (C) of OTX1/2 expression in hpNPCs and pan-NPCs. Arrowheads represent OTX^+ NPCs. *p = 0.022.

(D) Schematic of E12 telencephalon showing the cortical hem (red), DG (yellow), and CA primordia (green and blue).

(E) Wnt signaling pathway is upregulated in hpNPCs ($p_{adj} \leq 1.87E\text{-}06$)

(F) Schematic showing hCA3 differentiation paradigm.

(G) Arrowheads show $VGLUT1^+$ (red) and neuronal marker $NeuN^+$ (green) 4–5 WIV hCA3.

(H) Arrowheads show $GRIK4^+$ $MAP2^+$ neurons in hCA3 (4 WIV).

Results are presented as mean ± SEM. n = 3, *p < 0.05. Scale bar, 50 μm. See also Figure S1.

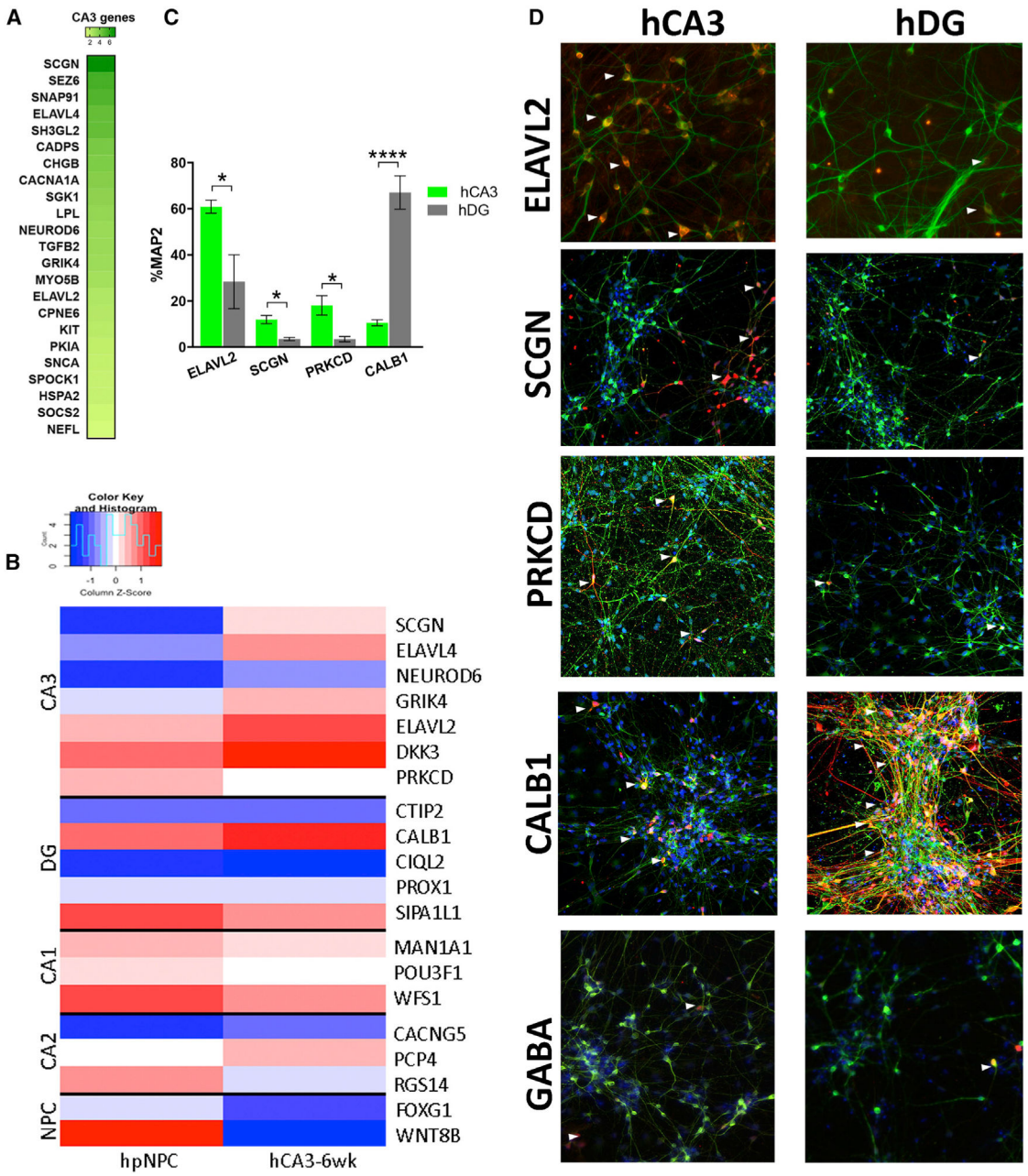

Figure 2. Comprehensive CA3 Patterning in hCA3 Protocol

(A)Heatmap showing $\log_2$ fold change in 23 CA3 genes hCA3 (3–6 WIV) and hpNPCs ($p_{adj} < 0.05$).

(B) Heatmap showing log2 fold change in expression of markers for CA3 (*Elavl2, Grik4, Neurod6, Scgn*, and *Dkk3*), CA2 (*Cacng5* and *Pcp4*), CA1 (*Pou3f1*), DG (*Prox1, Calb1, C1ql2*, and *Dock10*), and NPC (*Wnt 8b* and *Foxg1*) markers in hCA3 (6 WIV) and hpNPC ($p_{adj} < 0.01$).

(C and D) Immunostaining (D) and quantitation (C) of ELAVL2 (*p = 0.02), SCGN (*p = 0.01), PRKCD (*p = 0.02), CALB1 (****p < 0.0001), and GABA expression in hCA3 and hDG (4–5 WIV). Arrowheads show positive cells.

See also Figure S1.

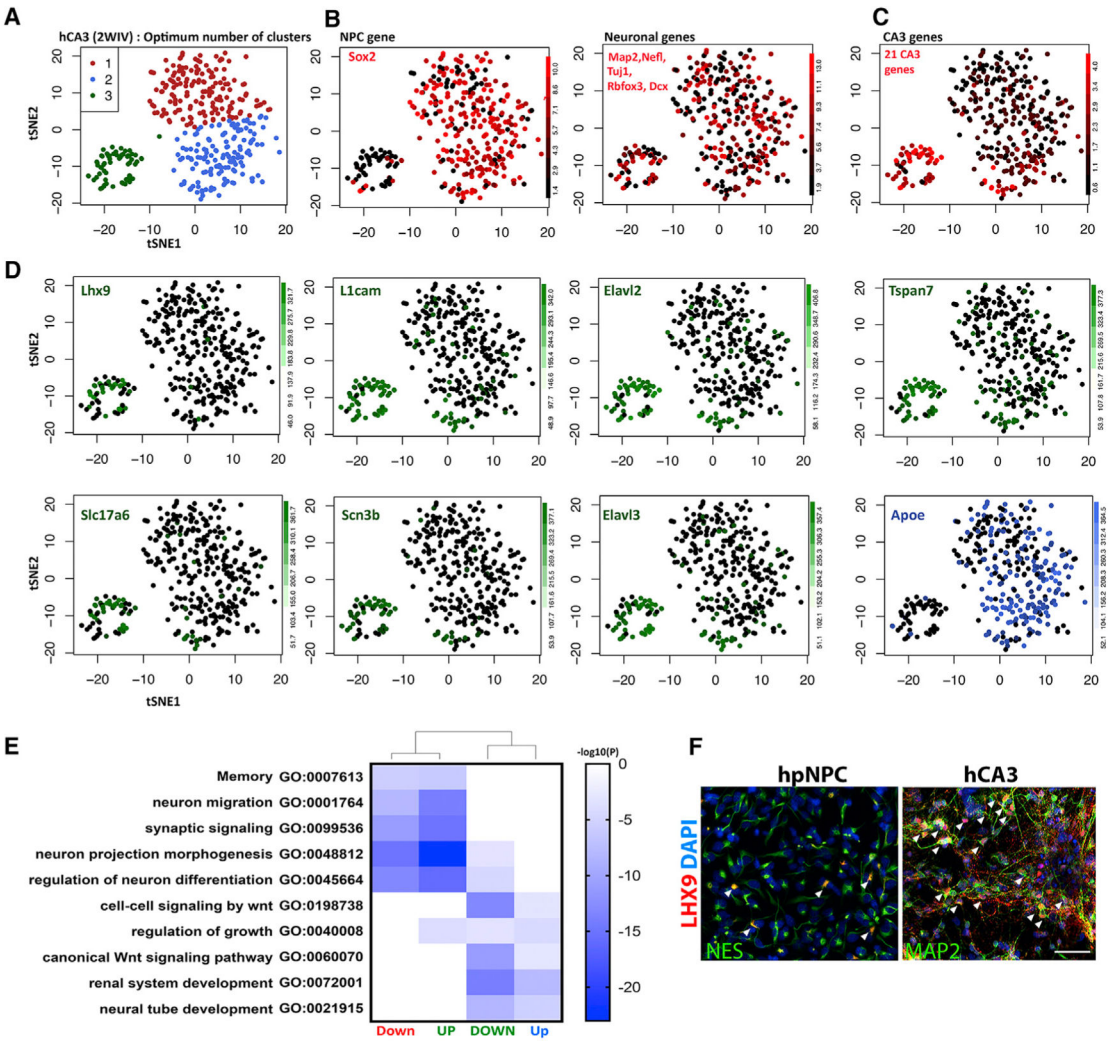

Figure 3. Molecular Census of hCA3 Neuronal Population

(A–D) tSNE plot showing 380 single cells (A) K-means clustering revealed 3 optimal numbers of clusters within the population (green, blue, and red).

(B) Average expression of neuronal genes (*Map2, Nefl, Tuj1, Rbfox3*, and *Dcx*) and *Sox2*. Red cells indicate expression; black indicates low or unidentifiable expression.

(C) Average expression of 23 CA3 genes is enriched in the green cluster.

(D) tSNE plot showing examples of DEGs (upregulatd: *Lhx9, L1cam, Elavl2, Tspan7, Vglut2* (*Slc17a6*), *Scn3b, Elavl3* and downregulated:*Apoe*) in the green cluster.

(E) Heatmap showing the enrichment analyses based on GO and KEGG pathways.

(F) Comparison of LHX9 expression (arrowheads) in hpNPC, hCA3 (4 WIV). Scale bar, 50 μm. See Figure S2.

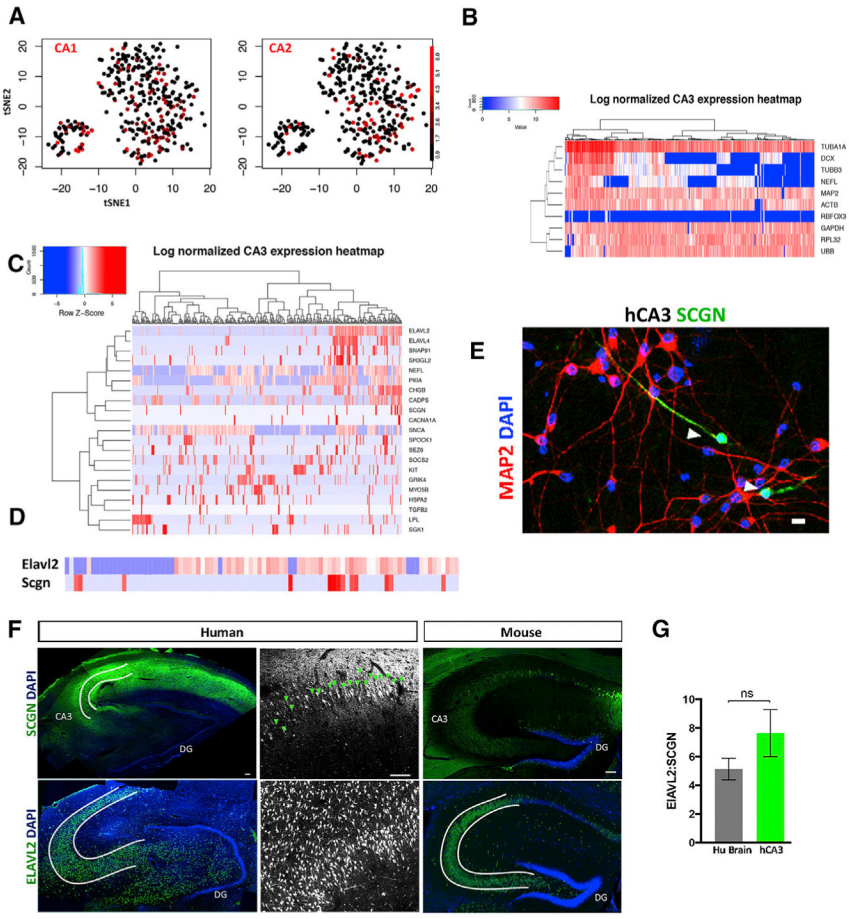

Figure 4. hCA3 Constitutes a Heterogeneous Population

(A) Expression of CA1 (*Wfs1* and *Pou3f1*) and CA2 genes (*Pcp4* and *Rgs14*)

(B and C) Heatmap showing expression of individual CA3 genes (B), as well as neuronal genes and housekeeping genes (C).

(D) *Elavl2* and *Scgn* (green) expression in green cluster cells)

(E) Sparse SCGN expression in the hCA3s (4 WIV). Scale bar, 10 μm.)

(F) SCGN is expressed (arrowheads) in human CA3, but not in mouse CA3. Scale bar, 50 μm.)

(G) Number of ELAVL2^{+}:number of SCGN^{+} ratio in human brain and hCA3s. ns, $p > 0.05$.)

See also Figure S3.

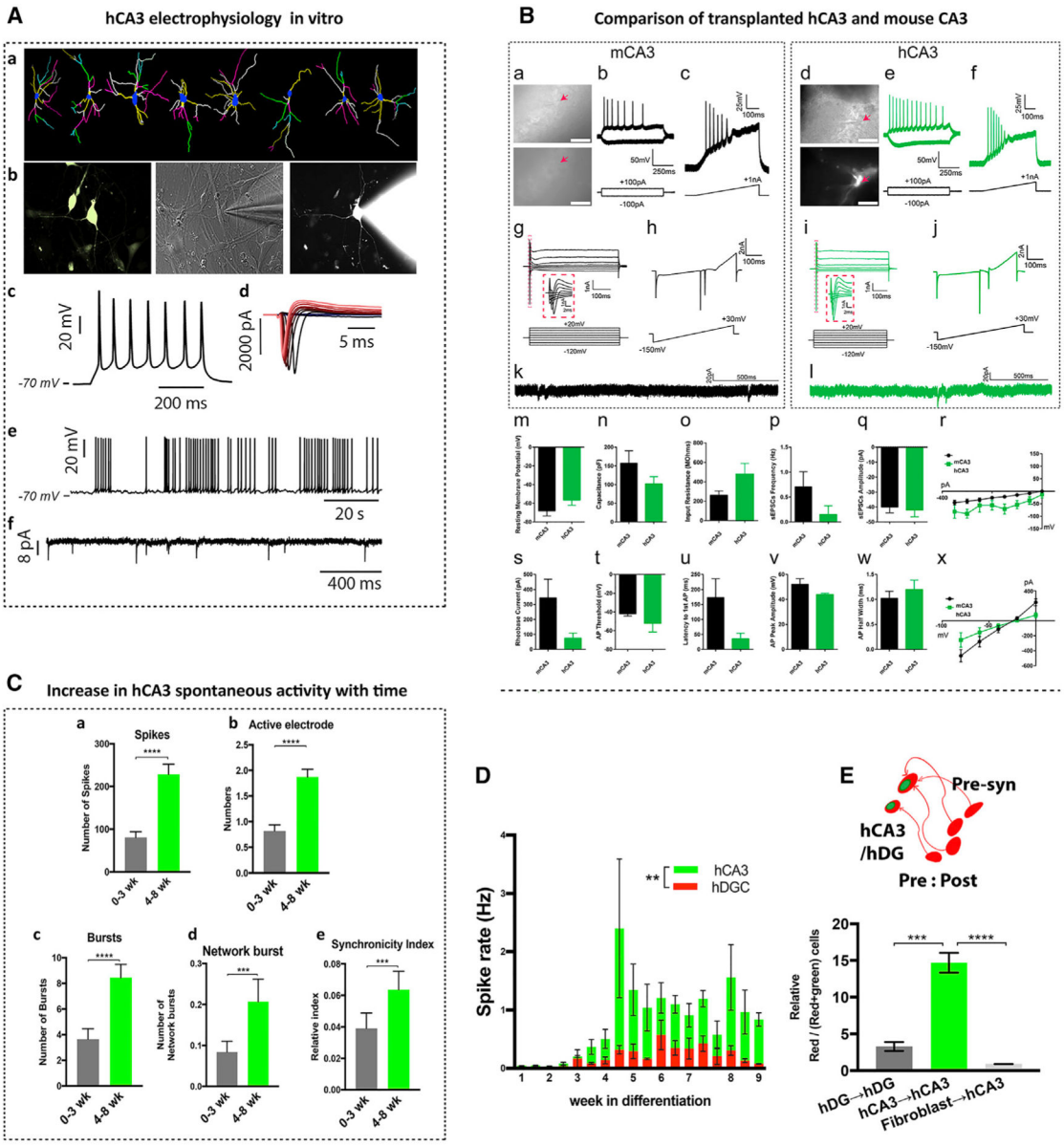

Figure 5. hCA3s Are Functionally Active

(A) Electrophysiology of hCA3s. (a) hCA3 morphology at 4 WIV. Dendrites are color-coded from yellow, white, magenta, and green to pale yellow to show consecutive branch orders. Scale bar, 10 μm. (b) Whole-cell patch clamping of eGFP^{+}hCA3 neurons (marked with lentiviral-Grik4-GFP or Elavl2-GFP reporter at 6 WIV). (c) An example of evoked AP (depolarizing step of 500 ms in current clamp). (d) Na^{+} and K^{+} current in response to a series of depolarizing steps in voltage clamp. (e and f) Examples of spontaneous AP in current clamp (e) and EPSCs recorded in voltage clamp (−70 mV) (f). See also Figures S4E–S4T.

(B) Comparison of transplanted hCA3s with mouse CA3 neurons. 7 mouse CA3s and 4 eGFP^{+}hCA3 neurons were recorded from mouse hippocampal slices at 3–3.5 MPT. (a and d) 40× images (top, differential interference contrast [DIC]; bottom, epifluorescence) of

patched mCA3 neurons(a) and hCA3 (d) in mouse brain slices. Scale bars, 100 μm. (b, c, e, and f) APs were evoked by somatic current injection steps (b and e) and ramps (c and f) in examples of a mCA3 (b and c) neuron and hCA3 (e and f). (g–j) Voltage steps (g and i) and ramps (h and j) elicit sodium spikes at depolarized potentials in an example of a mCA3 neuron (g and h) and hCA3 (i and j). (k and l) Spontaneous excitatory postsynaptic currents (sEPSCs) recorded from examples of mCA3 (k) and hCA3 neurons (l). (m) Resting membrane potentials (mV) ($p = 0.1760$), (n) capacitances (pF) ($p = 0.2196$), (o) input resistance ($p = 0.0596$), (p) sEPSC frequency ($p = 0.3236$), and (q) amplitude ($p = 0.7628$) of mCA3 and hCA3 neurons. (r) Current-voltage (IV) curves (generated from current injection steps) of mCA3 and hCA3 (repeated-measures two-way ANOVA, $F(1,7) = 4.442$, $p = 0.0731$, post hoc test multiple comparisons, Sidak's multiple comparison test, not significant at all points). (s–w) Rheobase or current injection needed to elicit first AP from ramp (pA) ($p = 0.2494$), AP threshold (mV) ($p = 0.1109$), latency to first AP (ms) ($p = 0.2438$), AP peak amplitude (mV) ($p = 0.3266$), or AP half-width (ms) ($p = 0.5140$) is not significantly different between mCA3 and hCA3 neurons. (x) Current-voltage (IV) curves (generated from voltagesteps) of mCA3 and hCA3 (repeated-measures two-way ANOVA, $F(1,7) = 0.4102$, $p = 0.5423$, post hoc test multiple comparisons, Sidak's multiple comparison test, not significant at all points. In (m)–(q) and (s)–(w), a two-tailed t test was performed. See also Figures S4E–S4T.

(C) Increase in spontaneous activity of hCA3 network with time (a–e). Number of spikes (****$p < 0.0001$) (a), active electrodes (****$p < 0.0001$) (b), bursts (****$p < 0.0001$) (c), network bursts (***$p = 0.0002$) (d), and synchrony index (***$p = 0.0008$) (e) over a 10-min MEA recording of hCA3s at 0–3 WIV (gray) versus 4–8 WIV (green). Number of recordings per group ≥ 7; number of neuronal cultures = 96.

(D) Spike rate (Hz) of hDG and hCA3s over a 10-min MEA recording. n = 3 neuronal cultures, recorded ≥2 times per week for 0–8 WIV and 1 time in the ninth WIV (**$p = 0.0071$).

(E) Schematic showing postsynaptic ($green^+red^+$) and presynaptic (red) neurons (left). hCA3 culture shows more connectivity (red^+/red^+green^+) compared to hDGs and mouse irradiated fibroblasts *in vitro* (right). ***$p = 0.0003$ and ****$p < 0.0001$.

Results are presented as mean ± SEM (recorded on 12-well MEA plate). See also Figure S3 and S4.

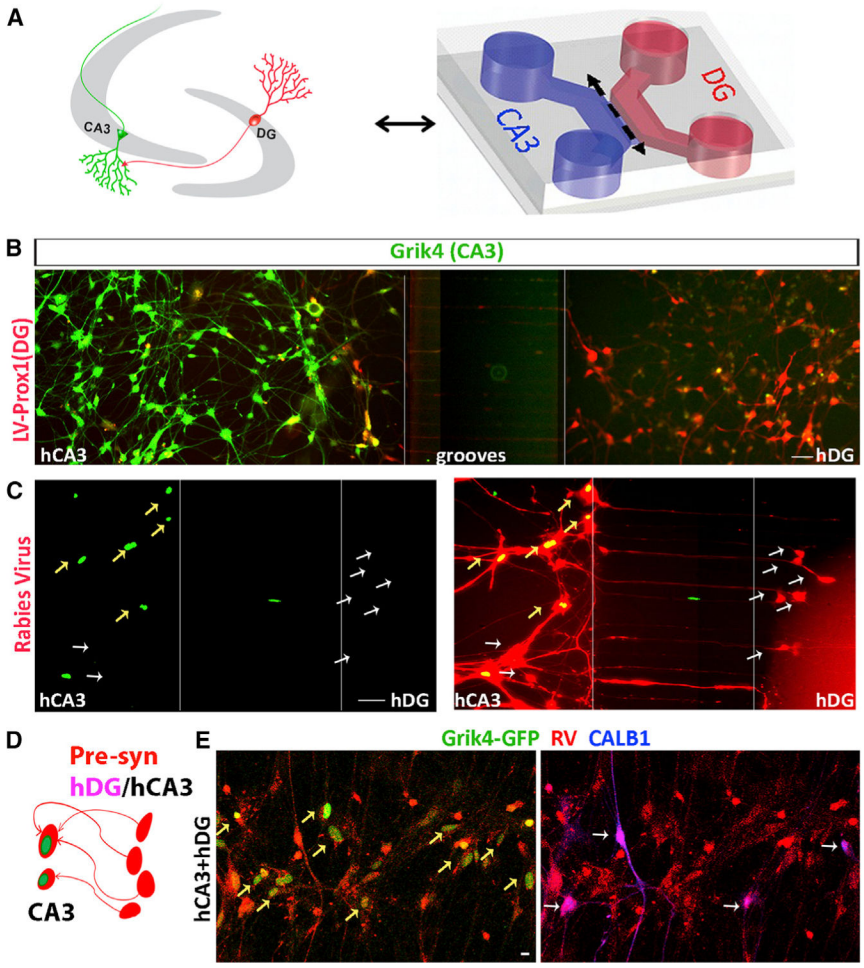

Figure 6. hCA3s Connect to hDGs

(A) Reconstruction of DG-CA3 neuronal connection (left) in microfluidic devices (right).

(B) hCA3s and hDGs were transfected with LV-Grik4-tdTomato (shown in green) and LVProx1-GFP (shown in red), respectively.

(C) Rabies tracing in microfluidic devices containing hCA3 (left) and hDG (right). Postsynaptic hCA3s (yellow arrows) are labeled with LV-Grik4-G-GFP (green; C, left) and rabies virus (green^{+}red^{+}; C, right); rabies virus traces the presynaptic cells (white arrows) in the DG compartment (red).

(D) Schematic showing postsynaptic (green^{+}red^{+}), presynaptic (red) and CALB^{+} presynaptic (red^{+}blue^{+}) neurons.

(E) hCA3s are marked CA3-specific LV-Grik4-GGFP (green, yellow arrow) in DG-CA3 co-culture in combination with rabies tracing (red). Immunostaining showing hCA3 (green^{+}red^{+}), presynaptic neurons (red), and CALB1^{+} (blue, white arrows) presynaptic neurons (red^{+}blue^{+}) as traced by rabies virus (red). Scale bar represents 50 μm in (B) and (C) and 10 μm in (E).

See also Figure S5.

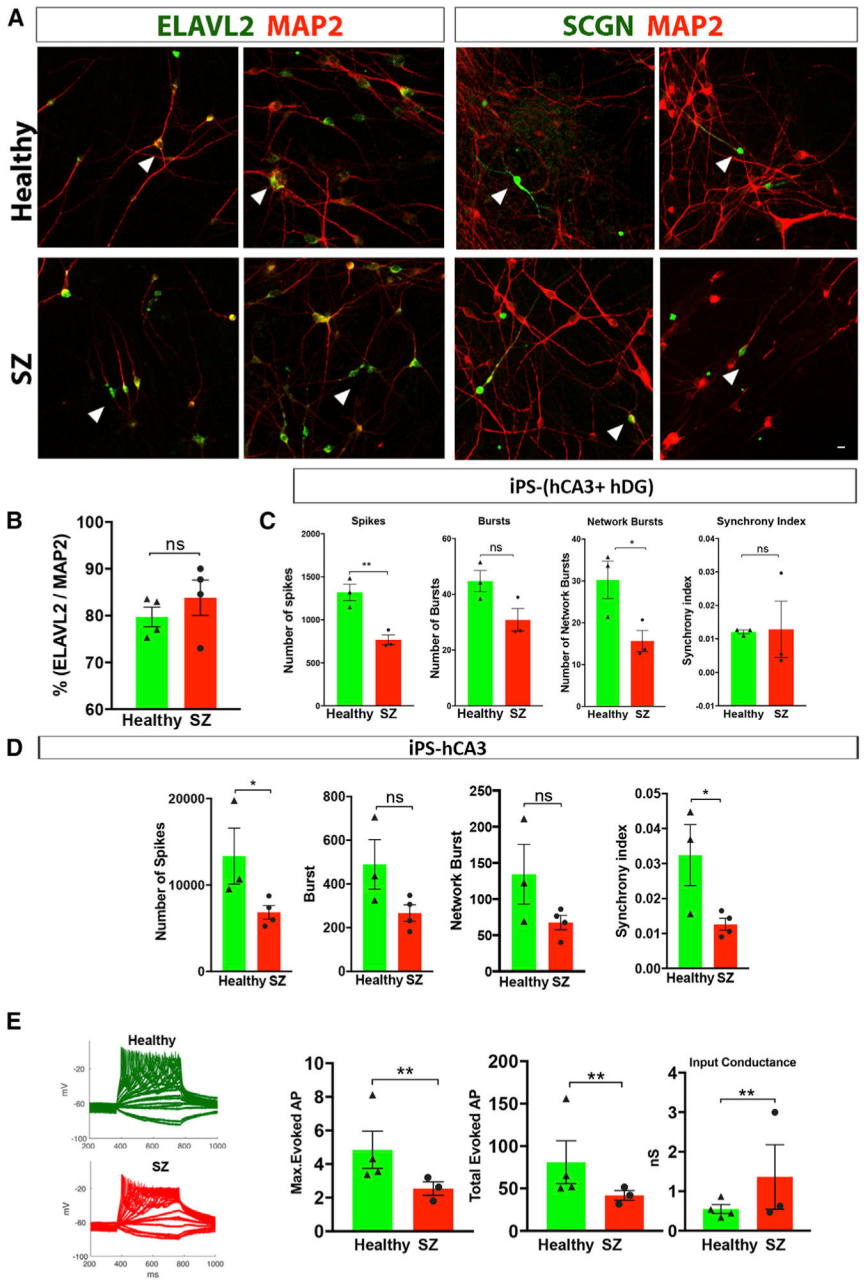

Figure 7. Reduced Spontaneous Activities in Hippocampal Neurons from a Cohort with SZ

(A) ELAVL2 (left, green, arrowheads), SCGN (right, green, arrowheads), and MAP2 (red) expression in hCA3s (4–5 WIV) from healthy and SZ patients. Scale bar, 10 μm.

(B) Numbers of ELAVL2^{+}MAP2^{+} neurons in healthy and SZ groups (n = 4 individuals per group; ns, p = 0.39).

(C) Reduced average spike (**p = 0.008) and network bursts (*p = 0.046) over 10 min of recordings in SZ-hCA3-hDG co-culture at 6 WIV. Bursts and synchrony index were not different (ns, p > 0.05). n = 12 neuronal cultures per individual).

(D) Reduced average number of spikes (*p = 0.04) and synchrony index (*p = 0.04) over a 10-min MEA recording of SZ-hCA3s (6 WIV). Number of bursts and network bursts were not different (ns, p > 0.05). n = 6 neuronal cultures per individual.

(E) Example of evoked APs from healthy (top) and SZ-hCA3 (bottom). At least 7 neurons per individual and a total of 73 neurons, including 40 neurons from the healthy cohort and 33 neurons from the SZ cohort, were analyzed. Total number (*p = 0.032) and maximum number of evoked Aps (**p = 0.008) were significantly reduced in hCA3 SZ at 4–5 WIV. Input conductance (nS) was increased in SZ-hCA3 (**p = 0.004).

Each dot shows an individual. Data are presented as mean ± SEM. n ≥ 3 iPSCs in healthy and SZ group. At least 3 (A, B, and E) or 6 (C and D) neuronal cultures per individual were used. ns, p > 0.05. Recordings were made on a 96-well MEA plate. See also Figures S6 and S7.

KEY RESOURCES TABLE

REAGENT or RESOURCE	SOURCE	IDENTIFIER
Antibodies		
Rabbit polyclonal anti-Calbindin	Swant	Cat#CB38
Rabbit polyclonal anti-Elavl2	Genetex	Cat# GTX12030
Rabbit polyclonal anti-Elavl2^{+}4	Abcam	Cat#ab72603, RRID:AB_1523538
Goat polyclonal anti-GFP	Abcam	Cat#ab6658
Goat polyclonal anti-Grik4 (KA1)	Santa Cruz biotechnology	Cat#sc-8917
Rabbit polyclonal anti-GABA	Sigma Aldrich	Cat#a2052
Rabbit polyclonal anti-Lhx9	Thermo Fisher scientific	Cat#PA5-52675
Chicken polyclonal anti-MAP2	Abcam	Cat#ab5392, RRID:AB_2138153
Mouse monoclonal anti-Nestin	Millipore	Cat# MAB5326
Mouse monoclonal anti-NueN	EMD Millipore	Cat#MAB377
Rabbit polyclonal anti-OXT1+ OTX2	Abcam	Cat#ab21990
Rabbit monoclonal anti- PRKCD	Abcam	Cat#182126
Rabbit polyclonal anti-SCGN	Thermo Fisher scientific	Cat# PA5-30393, RRID:AB_2547867
Rabbit polyclonal anti-Ctip2	Abcam	Cat# ab18465, RRID:AB_2064130
Rabbit polyclonal anti-Vglut1	Synaptic system	Cat#135303
Bacterial and Virus Strains		
Lentivirus vector pBOB-synP-HTB	Addgene plasmid	Cat#30195
Biological Samples		
Human postmortem brain samples	Shiley-Marcos Alzheimer's Disease Research Center brain bank (ADRC) at UCSD San Diego County Medical Examiner's Office	http://adrc.ucsd.edu
Human Genomic DNA	Promega	G1471
293T cells	ATCC	293T (ATCC) CRL-3216
Chemicals, Peptides, and Recombinant Proteins		
Accutase	StemCell Technologies	Cat#07920
BDNF	Peprotech	Cat#450-02
BDNF	R&D systems	Cat#248-BD
B-27 supplement	Thermo Fisher scientific	Cat#12587010
Collagenase IV	Thermo Fisher scientific	Cat#17104019
Cyclopamine	LC Laboratories	Cat#C-8700
Dibutyryl-cAMP	Tocris	Cat#1141
DAPI	Thermo Fisher Scientific	D1306, RRID:AB_2629482
DKK1	Humanzyme	Cat# HZ-7133
Dibutyryl-cAMP	Tocris	Cat#1141
Durcupan ACM single component A, M epoxy resin	Sigma-Aldrich	Cat#44611
FGF2	Joint protein central	Cat#1614

REAGENT or RESOURCE	SOURCE	IDENTIFIER
FGF2	Stemgent	Cat#03-0002
Ketamine	Putney	
Laminin Mouse Protein, Natural	Thermo Fisher scientific	Cat#23017015
L-ascorbic acid	Sigma-Aldrich	Cat#A4403
Matrigel	Trevigen	Cat#3432-005-01
Noggin	Humanzyme	Cat#HZ-1085
Noggin	Peprotech	Cat#120-10C
N-2 supplement	Thermo Fisher scientific	Cat#17502048
Picrotoxin	Millipore	Cat# 528105
poly-L-lysine mol wt 70,000–150,000	Sigma-Aldrich	Cat# P1274
Poly-L-ornithine	Sigma-Aldrich	Cat# P3655
Rock inhibitor	StemCell Technologies	Cat# 72308 Y-27632
SB431542	StemRD	Cat#SB-050
SB431542	Tocris	
WNT3a	R&D Systems	Cat#5036
Xylazine	Anased, Lloyd	sc-362950Rx
Critical Commercial Assays		
Agilent DNA 1000 Kit	Agilent	N/A
Phusion High-Fidelity DNA Polymerase	New England Biolabs	Cat#M0530S
Power SYBR Green PCR Master Mix	Thermo Fisher scientific	Cat#4368708
SureCell WTA 3′ Library Prep Kit for the ddSEQ System	Illumina	Cat#20014280
The High Capacity cDNA Reverse Transcription Kit	Thermo Fisher scientific	Cat#4368814
TruSeq Stranded Total RNA Library Prep kit	Illumina	Cat#20020597
Experimental Models: Cell Lines		
GM01792	Coriell Institute for Medical Research collection	Brennand et al., 2011
GM01835	Coriell Institute for Medical Research collection	Brennand et al., 2011
GM02038	Coriell Institute for Medical Research collection	Brennand et al., 2011
GM02497	Coriell Institute for Medical Research collection	Brennand et al., 2011
GM02937	Coriell Institute for Medical Research collection	Brennand et al., 2011
GM03651	Coriell Institute for Medical Research collection	Brennand et al., 2011
GM04506	Coriell Institute for Medical Research collection	Brennand et al., 2011
Hues6 hESC line (NIH approval number NIHhESC-09-0019)	HSCI	hES Cell Line: HUES-6
WT33	Marchetto et al., 2010	Agilent
293T human embryonic kidney cells	ATCC	CRL-3216
Experimental Models: Organisms/Strains		

REAGENT or RESOURCE	SOURCE	IDENTIFIER
NOD-SCID mice (NOD.CB17-*Prkdc*^{scid}/NCrHsd)	Envigo	N/A
C57BL/6NHsd	Envigo	N/A
Oligonucleotides		
Forward primer for Elavl2 5′-CTTTGGGAGCATTGGTGAAA-3′	This paper	N/A
Reverse primer for Elavl2 3′-TTCTCTGCATCCTTGGGGT-5′	This paper	N/A
Forward primer for Dkk3 5′- TCACATCTGTGGGAGACGAA-3′	This paper	N/A
Reverse primer for Dkk3 3′-GCTGGCAGGTGTACTGGAAG-5′	This paper	N/A
Forward primer for Pvrl3 5′-GCAAAGCTGTTACATTCCCG-3′	This paper	N/A
Reverse primer for Pvrl3 3′-CAGGCTCACAGTGGGTTCA-5′	This paper	N/A
Forward primer for Pvrl3 5′- CAAAGCTGTTACATTCCCGC-3′	This paper	N/A
Reverse primer for Pvrl3 3′-CAGGCTCACAGTGGGTTCA-5′	This paper	N/A
Forward primers for Gapdh 5′- TGCACCACCAACTGCTTAGC-3′	This paper	N/A
Reverse primer for Gapdh 3′- GGCATGGACTGTGGTCATGAG-5′	This paper	N/A
Recombinant DNA		
ELAVL2-EGFP (based on pCSC-GFP)	This paper	N/A
GRIK4-GFP (based on pCSC-EGFP)	This paper	N/A
pCSC-GRIK4-LL-HTB (based on vector pBOB-synP-HTB)	This paper	N/A
pBOB-synP-HTB	Addgene plasmid	Cat#30195
PROX1-EGFP	Yu et al., 2014	N/A
PROX1-5-EGFP	This paper	N/A
Deposited data		
Raw and analyzed RNA-seq data	This paper	GEO: GSE111979
Software and Algorithms		
Axion's Integrated Studio (AxIS) software (Neural activity)	Axion Biosystems	https://www.axionbiosystems.com/products/axis-software
Clampfit 9.0	Molecular Devices	N/A
pClamp 9 software	Molecular Devices	https://www.moleculardevices.com/systems/axon-conventional-patch-
Cutadapt (v.1.3)	*Python Software Foundation*	https://pypi.python.org/pypi/cutadapt
DESeq (v.1.16.0)	*Bioconductor*	https://bioconductor.org/packages/release/bioc/html/DESeq.html
HiSeq 2500 control software (HiSeq 2500 Sequencing System)	Illumina	https://www.illumina.com/systems/sequencing-platforms/hiseq-2500.
HOMER	Heinz et al., 2010	http://homer.ucsd.edu/homer/
HTSeq-count (v.0.5.4)	Anders et al., 2015	http://htseq.readthedocs.io/en/release_0.9.1/
ImageJ	NIH	https://imagej.nih.gov/ij/

REAGENT or RESOURCE	SOURCE	IDENTIFIER
MATLAB	MathWorks	https://www.mathworks.com/products/matlab.html
NeuralMetric Tool	Axion Biosystems	Axion Biosystems
Neurolucida Explorer	MBF Bioscience	http://www.microlucida.com/neurolucida
Real-Time Analysis software (HiSeq 2500 Sequencing System)	Illumina	https://www.illumina.com/systems/sequencing-platforms/hiseq-2500.l
SDS Software v 2.3 for 7900HT real-time PCR system	Thermo Fisher scientific	https://www.thermofisher.com/us/en/home/technical-resources/softwa
Sequencing Analysis Viewer software (HiSeq 2500 Sequencing System)	Illumina	https://www.illumina.com/systems/sequencing-platforms/hiseq-2500.l
STAR aligner (v.2.3.1o)	Dobin et al., 2013	https://github.com/alexdobin/STAR
ZEN Imaging Software	Carl Zeiss	https://www.zeiss.com/microscopy/int/products/microscope-software/
Other		
DMEM/F12 Glutamax	Thermo Fisher scientific	Cat#10565018
mTeSR1	StemCell Technologies	Cat#85850
Microfluidic devices	Kim et al., 2012	N/A